Psychosis-associated Valine to Leucine mutation in Neuregulin1 disrupts expression of a schizophrenia susceptibility gene network within the hippocampus and alters adult hippocampal neurogenesis.

Prithviraj Rajebhosale[1,9], Alice Jone[2,3,4,9], Kory Johnson[6], Camille Palarpalar[3,7,10], Samara Khan[3,7,10], Rohan Hoffland[3,7,10], Lorna W. Role[2,3,5], David A. Talmage[1,2,3,8]

[1] Genetics of Neuronal Signaling Section, National Institute of Neurological Disorders and Stroke, NIH, Bethesda, MD 20892, USA.
[2]Department of Neurobiology and Behavior, Stony Brook University, Stony Brook, NY 11794, USA.
[3] Center for Nervous System Disorders, Stony Brook University, Stony Brook, NY 11794, USA.
[4] Program in Neuroscience, Stony Brook University, Stony Brook, NY 11794, USA.
[5] Circuits, Synapses and Molecular Signaling Section, National Institute of Neurological Disorders and Stroke, NIH, Bethesda, MD 20892, USA.
[6] Bioinformatics Unit, National Institute of Neurological Disorders and Stroke, National Institutes of Health, Bethesda, MD 21042, USA.
[7] Undergraduate Biology Program, Stony Brook University, Stony Brook, NY 11794, USA.
[8] Department of Pharmacological Sciences, Stony Brook University, Stony Brook, NY 11794, USA.
[9] Co-first authors.
[10] These authors contributed equally.

Corresponding Author: David Talmage (David.Talmage@nih.gov)

Abstract

Schizophrenia is a complex genetic neurodevelopmental disorder. Expression quantitative trait loci (eQTLs) form the bulk of the genetic variation contributing to schizophrenia. Currently little is known about how eQTL expression is regulated or how this leads to the underlying cellular pathology. Neuregulin1-ErbB4 signaling plays a crucial role in synaptogenesis and has been implicated in schizophrenia. A psychosis-associated missense mutation in *NRG1* (rs74942016) is predicted to impair Nrg1 nuclear back-signaling, which is involved in transcriptional regulation and dendritogenesis, thereby implicating this mode of signaling in the underlying cellular pathology. We generated a transgenic mouse harboring the rs74942016 mutation in *nrg1*. We investigated the effect of this mutation ($V_{321}L$ in Type III Nrg1) on Nrg1 nuclear signaling. We performed transcriptomic analysis of the mutant dentate gyrus (DG) and identified several developmental processes predicted to be altered compared to wildtype DG. We assessed neurogenesis, cell cycle dynamics, fate commitment, and neuronal maturation *in vivo* in the mutant neurogenic niche. We found that the $V_{321}L$ mutation impairs nuclear translocation of the Nrg1 ICD. RNA sequencing identified cell cycle regulation, differentiation, neurogenesis, and dendritic growth as dysregulated processes in the mutant DG. We experimentally confirmed these predictions. Key nodes along the neurogenesis developmental timeline were found to be disrupted in the mutant DG, resulting in abnormal dendrite morphology and neural fate specification. We found that orthologs of known schizophrenia susceptibility genes were dysregulated in the mutant DG and interacted within a larger network of dysregulated genes in the mutant DG. Importantly, the schizophrenia-associated genes functioned as hubs coordinating this larger network, and the additional nodes within this extended network were functionally linked to known physiological processes and pathways associated with schizophrenia. Thus, our data show that Nrg1 nuclear back signaling is an important regulator of cell proliferation, neuronal specification, and maturation in the adult mouse DG. Loss of Nrg1 nuclear back-signaling due to the $V_{321}L$ mutation disrupts adult neurogenesis and results in dysregulation of a schizophrenia susceptibility gene network.

Introduction

Schizophrenia is a highly heritable neurodevelopmental disorder with complex genetic underpinnings. To date there have been ~270 genetic variants identified as schizophrenia susceptibility loci (Schizophrenia Working Group of the Psychiatric Genomics Consortium, Ripke, Walters, & O'Donovan, 2020). Genetic variation in schizophrenia risk involves few causal rare variants with large effect sizes, as well as common variation with low effect sizes (Hong Lee S., et al. 2012; McClellan J & King M-C. 2010). Most common risk-associated variants are expression quantitative trait loci (eQTL) that influence risk by altering expression of genes through mechanisms that remain poorly understood (Richards AL., et al. 2012). However, mechanistic understanding of how genetic risk contributes to disease pathology remains unclear.

Several studies examining functional enrichment of associated genes have concluded that genes associated with neurodevelopmental signaling pathways, in particular synaptogenesis, underlie dysfunction in schizophrenia (Schizophrenia Working Group of the Psychiatric Genomics Consortium, Ripke, Walters, & O'Donovan, 2020; Wang Q., et al. 2019). Among these is the Neuregulin 1 (NRG1)-ERBB4 signaling axis (Li R., et al. 2020; Walsh T., et al. 2008; Harrison PJ. & Weinberger DR. 2004). The *NRG1* gene has been associated with schizophrenia in several populations (Kukshal P., et al. 2013; Alaerts M., et al. 2009; Shiota S., et al. 2008; Harrison PJ. & Law AJ. 2006; Stefansson H., et al. 2002). The functional significance of NRG1 signaling to the predicted pathology, and observations from several rodent models of Nrg1 dysfunction beckon further investigation into the intersection of NRG1 signaling with schizophrenia risk.

The *nrg1* gene encodes more than 31 different protein isoforms that are generated via alternative splicing and differential 5' exon usage (Falls DL. 2003). These isoforms can be generally divided into 2 groups – ones that contain an immunoglobulin-like domain (Ig-Nrg1) and ones that have a cysteine-rich domain (CRD-Nrg1). While Nrg1 proteins are more widely known as ligands for ErbB family receptor tyrosine kinases, Type III Nrg1, a CRD-containing isoform, is unique in that it has been shown to participate in bidirectional signaling, *i.e.,* acting as both a ligand and a receptor for ErbB4 (Talmage DA. 2008; Bao J., et al. 2003). Type III Nrg1 hypomorphic mice show several circuit and cellular pathologies associated with schizophrenia, such as sensorimotor gating deficits and deficits in axonal and dendritic growth (Chen Y-JJ., et al. 2008, Chen Y et al. 2010). Upon binding ErbB4, the Type III Nrg1 C-terminal intracellular domain (ICD) can engage local phosphatidylinosiltol 3-kinase (PI3K) signaling (local back-signaling) (Hancock ML., et al. 2008) and/or the C-terminal transmembrane domain (TMc) can undergo proteolysis by the γ-secretase enzyme complex resulting in translocation

of the free ICD to the nucleus (nuclear back-signaling) (Bao J., et al. 2003). The nuclear ICD is predicted to regulate gene expression given its strong transactivation properties and reports of interactions with transcriptional regulators (Pirotte D., et al. 2010; Bao J., et al. 2004; Bao J., et al. 2003).

A missense mutation in *NRG1* resulting in a single amino acid change in a transmembrane valine to leucine (rs74942016- results in Val→Leu at position 321 in Type III Nrg1 β1A) was associated with schizophrenia and psychosis in a Costa Rican population (Walss-Bass C., et al. 2006). Intriguingly, γ-secretase cleaves Nrg1 between residues cysteine 320 and valine 321, and $V_{321}L$ substitution results in impaired cleavage and reduced nuclear translocation of the ICD (Fleck D., et al. 2016; Fleck D., et al. 2015; Chen Y., et al. 2010). Additionally, previous reports showed that impaired γ-secretase processing of Nrg1 contributes to endophenotypes of schizophrenia in animal models (Fazzari P., et al. 2014; Dejaegere T., et al. 2008). Type III Nrg1 and its receptor/ligand ErbB4 are both synaptic proteins (Exposito-Alonso D., et al. 2020; Vullhorst D., et al. 2017; Fazzari P., et al. 2010). Synaptic interactions are likely regulators of nuclear back-signaling, placing this mode of signaling in a disease-relevant neurodevelopmental window. Taken together, we hypothesize that impaired nuclear function of the Nrg1 ICD contributes to schizophrenia susceptibility.

In this study, we investigated nuclear back-signaling by the Nrg1 ICD and its effects on the dentate gyrus transcriptome by generating transgenic mice harboring the psychosis-associated $V_{321}L$ mutation in Nrg1. Hippocampal dysfunction is one of the most consistently described features in both human and animal studies of schizophrenia (Hu N., et al. 2020; Provenzano FA., et al. 2020). The dentate gyrus (DG) serves as the gate for incoming information into the hippocampus, and structural and functional alterations in the DG have been implicated in schizophrenia, with unique eQTL signatures in the DG that are not detected in hippocampal homogenates (Hu N., et al. 2020; Nakahara S., et al. 2020; Jaffe et al. 2020; Walton NM., et al. 2012). Additionally, given the presence of the adult neurogenic niche, the DG provides a unique opportunity to simultaneously assess effects of the V321L mutation on cells in various stages of development and maturation. Thus, we chose the DG as a candidate region to begin investigating the effects of impaired gamma-secretase processing of Nrg1.

Results

Generation of the *nrg1* $V_{321}L$ mutant mouse model to study γ-secretase-mediated NRG1 signaling

To examine the effect of a Val-321-Leu substitution ($V_{321}L$) on Type III Nrg1 signaling *in vivo*, we generated a knock-in germline mutation in mice. The $V_{321}L$ mutation (gtg→ttg) was introduced into C57Bl6 ES cells using a bacterial artificial chromosome (BAC) construct (**Figures 1A-D**). Heterozygotes were interbred, and offspring were born at the expected Mendelian ratios (**Figure 1E**). Homozygous $V_{321}L$ mutants (MUT) were viable and fertile, with no outward morphological or growth abnormalities. Homozygous animals were able to interbreed and yielded normal-sized litters with offspring that appeared healthy. The $V_{321}L$ mutation is also viable on a Type III Nrg1 knock-down background, as a *Nrg1*$^{L/L}$ x Type III *Nrg1*$^{+/-}$ cross yielded both *Nrg1*$^{V/L}$ and *Nrg1*$^{L/-}$ offspring.

$V_{321}L$ mutation disrupts cleavage by gamma secretase and leads to reduced NRG1 nuclear signaling.

We performed subcellular fractionation to isolate nuclei from cortical and hippocampal lysates of $V_{321}L$ homozygous mutant (MUT) and their wildtype (WT) litter- and cage-mates and compared the levels of Nrg1 ICD by immunoblot analysis (**Figure 2A**). Nuclei isolated from MUT animals showed lower levels of Nrg1 ICD compared to nuclei from wildtype counterparts, consistent with diminished Nrg1 nuclear signaling in the mutant cortex and hippocampus.

Type III Nrg1 back-signaling results in the appearance of distinct clusters of the ICD in the nucleus (Bao J., et al. 2003). To determine whether nuclear ICD clusters were altered in neurons from MUT mice, we cultured dispersed hippocampal neurons from postnatal day 4 (PND 4) WT and MUT mice (culture age:17 days *in vitro* (DIV)). To assess the composition of our cultured hippocampal neurons, we immunostained for the dentate gyrus marker Prox1 along with βIII Tubulin (TuJ) to identify all neurons (**Figure 2B**). We found ~70% of the neurons were dentate granule cells (Median: 69.1% ± 0.02% std. dev). We stimulated these cultures with soluble recombinant ectodomain of ErbB4 (sB4) and quantified nuclear ICD clusters (**Figure 2C left**). We found that stimulation with sB4 increased number of nuclear ICD clusters in neurons from WT mice (**Figure 2C right;** WT Veh v. WT sB4 One-way ANOVA Bonferroni adj. $p<0.0001$). This increase in nuclear ICD clusters was blocked by pre-treatment with the γ-secretase inhibitor, DAPT (**Figure 2C right;** WT Veh v. WT (sB4) + DAPT Bonferroni adj. $p>0.9999$). We did not observe increased nuclear ICD clusters following treatment with sB4 in neurons from MUT mice (**Figure 2C right;** MUT Veh v. MUT (sB4) Bonferroni adj. $p>0.9999$). There was no difference in nuclear clusters at baseline between WT and MUT neurons (WT Veh v. MUT Veh Bonferroni adj. $p>0.9999$).

Changes in Nrg1 $V_{321}L$ mutant transcriptome point to aberrant neurogenesis, cell cycle dynamics, and dendrite development.

The Nrg1 ICD has strong transactivation properties (Bao J., et al. 2003). MUT mice have impaired nuclear translocation of the ICD. Thus, we predicted that impaired nuclear signaling by the

Nrg1 ICD would result in transcriptomic changes. We examined the transcriptomes of isolated dentate gyri (DG) from WT and MUT mice using RNA sequencing (RNA-Seq).

We extracted RNA from microdissected DG from 2-month-old WT and MUT mice (**Figure 3A**). mRNA was enriched via poly-A selection and sequenced on an Illumina NGS platform. Following sequencing, data were quality-controlled (QC), normalized via noise modelling and noise reduction scaling, inspected via PCA clustering, and corrected for any batch and sex effects (see methods for details). Following differential gene expression analysis, we found 1312 significantly dysregulated genes (colored dots, ANCOVA corrected $p \leq 0.1$ and linear fold change of ±1.25) between WT and MUT mice (**Figure 3B; Table S1**).

To identify possible functional alterations that might result from transcriptional dysregulation in the MUT mice, we used ingenuity pathway analysis (IPA) to find cellular features regulated by the most significantly dysregulated genes in our dataset. Several functions along the neurodevelopmental trajectory were predicted to be disrupted in MUT DG, including cell proliferation, differentiation, maturation, and dendrite development, (**Figure 3C**). We found that the DG-specifying transcription factor *prox1* and mature granule cell marker *calb1* were both downregulated in our transcriptomic analysis. To confirm this, we performed immunohistochemistry on WT and MUT DG brain sections and quantified Prox1 and Calb1 protein expression in the granule cell layer of the dorsal DG (**Figure 3E**). We found significantly lower immunostaining of Prox1 and Calb1 in the MUT DG compared to WT (**Figure 3E right**, Prox1: WT v. MUT $p=0.029$ Mann-Whitney Rank Sum Test, $U=0$; Calb1: WT v. MUT $p=0.029$ Mann-Whitney Rank Sum Test, $U=0$).

Disease annotations in IPA indicated that dysregulated genes in the MUT mice were enriched in schizophrenia-susceptibility genes, indicating that the $V_{321}L$ mutation alters the transcriptional landscape in ways that have been associated with the genetic architecture of schizophrenia (**Figure 3D**). We also found that dysregulated genes in the MUT mice were enriched in cancer-associated genes, indicating a potential relationship with regulation of cell proliferation.

We next asked whether the differentially expressed genes shared transcriptional regulatory mechanisms. (Lachmann A., et al. 2010; Chen EY., et al. 2013; Kuleshov MV., et al. 2016; Xie Z., et al. 2021). We performed this analysis separately for up- and down-regulated genes. We identified that the 664 significantly upregulated genes in MUT mice were enriched for genes predicted to be regulated by members of the polycomb repressor complex 2 (PRC2) (Suz12, Ezh2), RE1-Silencing Transcription factor (REST), Smad4, CCCTC-binding factor (CTCF), structure maintenance of chromosome 3 (Smc3), doublestranded break repair protein (Rad21), and nuclear factor erythroid-derived 2-like 2 (Nfe2l2) (**Figure S3A**). We found that 126 of the 664 genes were targets for regulation by the PRC and ~35% of the REST target genes were also targets for the PRC. Gene ontology analyses for these PRC-target genes revealed that they were involved in positive regulation of neuronal differentiation and negative regulation of cell proliferation (**Table S2**). Intriguingly, we found that Ezh2 and Eed (catalytic subunits of PRC) were downregulated in the RNASeq comparison between WT and MUT DG (**Table S1**). Taken together with the ontology analysis of the predicted PRC-regulated genes in our dataset, we predict that loss of proper repression by the PRC might result in suppression of neural stem cell proliferation in the DG and a push toward differentiation.

The 647 downregulated genes showed strongest enrichment of genes predicted to be regulated by the transcription factor E2f4 (odds ratio: 3), followed by TATA-Box Binding Protein Associated Factor 1 (Taf1), Upstream Binding Transcription Factor (Ubtf), Zinc Finger Protein 384 (Znf384), Myc-associated Factor X (Max), Sin3 Transcription Regulator Family Member A (Sin3A), and Early Growth Response 1 (Egr1) (**Figure S3B**). These E2f4-target genes were found to be involved in mitotic spindle

organization, chromatin remodeling, RNA-splicing, and regulation of ribosomal synthesis (**Table S2**). Overall, the downregulated genes were found to be involved with positive regulation of mitosis.

Taken together these changes strongly indicate reduction in proliferation within the MUT neurogenic niche and increased differentiation towards the neuronal fate.

Type III Nrg1 is expressed in subgranular zone neural progenitors, and the granule cell layer in the dentate gyrus.

$V_{321}L$ mice show reduced nuclear back signaling and transcriptomic changes in the DG, consistent with a predicted effect on several neurodevelopmental processes in the neurogenic niche. We next asked where in the DG is Nrg1 expressed.

We found that Type III Nrg1 transcripts were widely expressed within the DG, particularly within the subgranular zone (SGZ) and the granule cell layer (GCL) (**Figure 4A**). Next, we performed immunohistochemistry (IHC) with an antibody (NeuroMAb #75-226) targeting the unique Type III Nrg1 N-terminal domain. IHC for Type III Nrg1 revealed its expression in the mouse hippocampus proper (**Figure 4B left**). In the DG, we observed Type III Nrg1 protein throughout the granule cell layer, with punctate staining in the molecular layer (**Figure 4B right; inset**). In the neurogenic niche, Type III Nrg1 immunoreactivity was observed in cells located on the border of the hilus and the granule cell layer (**Figure 4B right; inset**). Subpopulations of cells in the hilus also appeared to express Type III Nrg1 (**Figure 4B right; inset**).

Next, we asked if Type III Nrg1 was expressed in neural progenitors in the DG. We labelled proliferative cells with EdU, a thymidine analogue that is incorporated into cells undergoing DNA synthesis (Altman, J. & Das, G. D. 1965; Ming, G.-l. & Song, H. 2005) and stained brain sections for Type III Nrg1 24 hrs later. We found that subsets of EdU-positive cells in the dentate gyrus expressed Type III Nrg1 (**Figure 4C**). We also performed co-immunohistochemistry with an antibody targeting doublecortin (Dcx), a microtubule-associated protein expressed by neuroblasts and immature neurons in the dentate gyrus. Type III Nrg1 expression colocalized with that of Dcx, although not all Dcx-positive cells expressed Type III Nrg1 (**Figure 4D**).

Abnormal progenitor pool maintenance and differentiation in the $V_{321}L$ mutant dentate gyrus.

To assess overall neurogenesis in the hippocampus, we examined the proliferative cell population in the MUT DG using Ki67, a marker for cells in cell cycle (**Figure 5A**). Stereological analysis revealed a statistically significant decrease in the proliferative population in MUT animals compared to WT (**Figure 5A**; p= 0.0271, Welch's t-test).

To quantify newborn neuron production in the hippocampus, we performed immunohistochemistry for the immature neuron marker, doublecortin (Dcx) (**Figure 5B**). Dcx+ cell counts were comparable between MUT and WT animals at ages 2-months, 4-months, and 6-months old, shown pooled here in **Figure 5B** (p=0.9865, Welch's t-test). Thus, proliferation was stunted in the

MUT DG, although this impairment did not result in a difference in the number of newborn neurons produced.

The discrepancy between decreased proliferation and unchanged neuronal production in the MUT DG could be explained by disruptions to the balance between self-renewal maintenance and postmitotic neuronal differentiation, both of which are processes predicted to be disrupted by the $V_{321}L$ mutation based on IPA of the transcriptomic data (**Figure 3C)**. Therefore, we asked whether cell cycle dynamics and fate commitment by neural stem cells are abnormal in the MUT DG.

To measure the rate of cell cycle reentry, proliferative cells in the S phase of cell cycle were first labelled by systemic introduction of EdU (50µg/g body weight). 24 hours after EdU injection, brains sections were collected to probe for Ki67 expression. If a cell, proliferative at the time of EdU injection had re-entered the cell cycle after 24 hours, it would be EdU+ and Ki67+. Conversely, if the cell had exited the cell cycle, it would only be EdU+. The overall rate of cell cycle reentry can then be measured as the proportion of total EdU+ cells that are also Ki67+. We observed a statistically significant decrease in cell cycle re-entry in the MUT DG compared to WT DG (**Figure 5C**; p= 0.0043, Mann-Whitney Rank Sum Test). This could mean that the self-renewing pool of neural progenitors was depleted faster in the MUT DG, generating more postmitotic cells in the dentate gyrus.

Given the higher rate of cell cycle exit in MUT DG, we asked if fate programming was affected. MUT and WT DGs were stereotaxically injected with a replication-deficient retrovirus expressing GFP, which only stably infects cell during mitosis, resulting in GFP expression in their progeny. After 14 days to allow for neural stem cell proliferation and/or differentiation (Bond AM., et al. 2015; Jahn, H. M. & Bergami, M. 2018), brains were collected for identification of GFP+ progeny. The identity of GFP+ cells were determined by a combination of morphology, Dcx immunoreactivity, and Nissl staining. Neural progenitors were identified by short, tangential processes and the lack of radially oriented processes, with or without Dcx immunoreactivity (**Figure 5D**, open arrowheads). Immature granule cells were identified by their radially oriented neurites and Dcx+ Nissl+ staining (**Figure 5D**, closed arrowheads). Astrocytes were identified by their star-like morphology, extensive branch ramifications, and lack of Dcx immunoreactivity and Nissl staining (**Figure 5D**, yellow arrows).

The results revealed a decrease in the proportion of neural progenitors in the MUT DG compared to WT DG (**Figure 5D**; Two-way ANOVA Genotype x Cell Fate p=0.0003 F (3, 20) =9.864. NP, WT v. MUT Bonferroni-corrected p=0.0026), consistent with the observed depletion of the proliferative pool (**Figure 5A**) and increased rate of cell cycle exit (**Figure 5C**). Interestingly, fate commitment in the MUT DG was disproportionately biased towards the neuronal fate program compared to astroglial fate (**Figure 5D**; iGC, WT v. MUT Bonferroni-corrected p=0.0069). In fact, the proportion of astrocytes generated by the mutant neural stem cells was not significantly different between MUT and WT DG (Astrocyte, WT v. MUT p>0.9999).

Thus, MUT neural stem cells display decreased self-renewal maintenance and a selective increase in neuronal fate commitment, suggesting Nrg1 nuclear signaling may instruct neural stem cell self-renewal maintenance and neurogenesis without participating in astrogliogenesis. Additionally, 1-month EdU pulse-chase experiments suggests that survival of neural progenitors and newborn neurons is modestly increased in MUT DG (**Figure S5**). The depletion of the proliferative neural stem cell pool, increased cell cycle exit, and disproportionate production of neurons over astrocytes in the MUT DG point to an essential role for NRG1 ICD nuclear signaling in neural stem cell maintenance and fate commitment in the adult mouse DG.

The NRG1 $V_{321}L$ mutation compromises neuronal maturation of granule cells in the dentate gyrus

Since neuronal fate commitment and development is a fine-tuned process, we asked whether disruption to neural stem cell self-renewing properties and the accelerated rate of neuron production in the MUT DG resulted in abnormal neuron development and maturation. Nrg1 nuclear back-signaling has already been demonstrated to be important for neuronal development, with an essential cell-autonomous role in dendrite arborization and spine production (Chen Y., et al. 2010; Fazzari P., et al. 2014). RNASeq analysis of the MUT DG shows dysregulation of genes involved in dendrite development (**Figure 3C**). Therefore, we examined the dendrite morphology of newborn dentate granule cells.

Qualitative observations from Dcx immunohistochemistry revealed a notable decrease in dendritic complexity of adult-born immature neurons in MUT DG. Dcx immunostaining also tended to be weaker in the mutant molecular layer, into which the granule cells extend their dendrites (**Figure 6A, right insets**).

To quantify dendritic arborization of granule cells in the dentate gyrus, we used Golgi impregnation to visualize neuronal morphology and analyzed dendrites of neurons with typical granule cell morphologies in NeuronStudio (see methods for details). **Figure 6B** shows two representative tracings of granule cells from each genotype. Total dendritic length was modestly greater in MUT mice, although this difference was not statistically significant (**Figure S6-1A**). Sholl analysis revealed significant increases in MUT dendritic length proximal to the soma (**Figure 6C**; at 80μm away from soma Bonferroni-corrected p=0.052, Two-way RM ANOVA with a significant (Genotype x Distance from soma) interaction p=0.0347).

Furthermore, dendrite complexity appeared to be compromised in granule cells sampled from MUT DGs. Most of the dendritic length appeared to be distributed in 4th and 5th order branches in WT granule cells, while in MUT granule cells, the peak of dendritic mass was found in 4th order branches with less mass distributed in 5th order branches (**Figure 6D**, 5th order branching: Bonferroni-corrected p= 0.055, Two-way ANOVA). In fact, there was a statistically significant decrease in the proportion of granule cells that possessed 5th order branching in MUT granule cells, and while a small percentage of WT granule cells possessed 6th and 7th order branches, these high order branches were not observed in MUT granule cells (**Figure 6E**, 5th order: p= 0.0131, 6th order: p= 0.0815, 7th order: p= 0.458, Fisher's exact test). Total number of branch points was not significantly altered in the MUT DG (**Figure S6-1B**).

Altogether, examination of dentate granule cells revealed subtle but significant impairment in the development of dendrites in MUT granule cells, especially in distal dendrites. Thus, diminished NRG1 nuclear back-signaling results in persistent and cumulative effects on dendrite growth and complexity across development.

Type III Nrg1 back-signals via two known mechanisms – 1. Local axonal, PI3K signaling and 2. γ-secretase-dependent nuclear signaling (Bao J., et al. 2003; Hancock M., et al. 2008; Chen Y., et al. 2010). Type III Nrg1 KO cortical neurons in culture show defects in both axonal and dendritic outgrowth and branching. Nuclear signaling-incompetent forms of Nrg1 (i.e., those lacking the nuclear localization signal (NLS) or $V_{321}L$ mutant) rescue defects in axonal growth, but are unable to rescue defects in dendritic growth, indicating that Type III Nrg1 nuclear signaling is necessary for proper dendrite maturation in cortical neurons but dispensable for axon outgrowth (Chen Y., et al. 2010; Fazzari P., et al. 2014). We asked whether neurons from MUT mice are selectively deficient in dendrite development

in response to sErbB4 stimulation. Cortical neurons from embryonic (E18.5) WT and MUT mouse pups were cultured for 3 days and treated with sErbB4 with or without pharmacological inhibition of PI3K using Wortmannin (WM) or γ-secretase using L-685,458 (L6).

Neurons from WT mice showed increases in axonal and dendritic length in response to sErbB4 treatment which were blocked by WM and L6 respectively (**Figure S6-2A and S6-2B navy blue boxes**; axonal length: WT NT v. WT One-way ANOVA sB4 p=0.0002; dendritic length: WT NT v. WT sB4 p=0.0019). WM treatment did not block sErbB4-induced dendritic growth and L6 treatment did not prevent sErbB4-induced axonal growth (axonal length: WT L6 v. WT L6+sB4 p<0.0001; dendritic length: WT WM v. WT WM+sB4 p<0.0001). These results demonstrate and agree with published data showing that Nrg1 nuclear back-signaling influences dendritic growth (Chen Y., et al. 2010; Fazzari P., et al. 2014). They also establish that ErbB4-stimulation of axonal growth requires PI3K signaling.

sErbB4 treatment stimulated axon growth in neurons from MUT mice which was blocked by WM treatment and not by L6 (**Figure S6-2A light blue boxes**; axonal length: MUT NT v. MUT sB4 One-way ANOVA p=0.0014, MUT WM v. MUT WM+sB4 p=0.1113, MUT L6 v. MUT L6+sB4 p=0.0289). Notably, MUT neurons did not show increases in dendritic length in response to sErbB4 stimulation (**Figure S6-2B** dendrite length: MUT NT v. MUT sB4 p>0.9999). These results indicate that PI3K signaling-dependent axonal growth is intact in $V_{321}L$ mutant mice, whereas γ-secretase-dependent dendritic growth is selectively disrupted.

Dysregulation of a functionally connected schizophrenia susceptibility gene network in the LL DG.

The $V_{321}L$ mutation was identified originally as being associated with psychosis and schizophrenia (Walss-Bass C., et al. 2006). The disease annotations of dysregulated genes in the LL mouse DG indicated an enrichment of schizophrenia-associated genes (**Figure 3D**). Thus, we created a merged network of dysregulated genes in the LL DG whose human orthologs are associated with psychosis, schizophrenia, sporadic schizophrenia, or schizoaffective disorder, under the umbrella term of “schizophrenia spectrum disorders” (**Figure 7A left;** p≤0.0005). We then grew this network by providing the dataset of the significantly dysregulated genes in the MUT DG seeking to find genes in our dataset that have not been explicitly identified as schizophrenia-associated but might have functional interactions with dysregulated schizophrenia-annotated genes. This resulted in a network with 322 nodes and 371 edges (**Figure 7A, right**). Pathway analysis shows that this gene network is significantly enriched for genes that are associated with neurotransmitter/modulator synapses, chemokine signaling, AKT signaling, and nicotine addiction, which are functions/pathways implicated in the pathology underlying psychotic disorders (**Figure 7B**).

Analysis of the schizophrenia-susceptibility network showed that the degree of a node and its topological coefficient were inversely related, i.e., a highly connected node in this network does not share neighbors with its connected nodes (Data not shown). This indicates the presence of a “hub and spoke” network topology wherein hub nodes interact preferentially with a few other nodes as opposed to with each other. To gain further insight into this, we identified hub nodes using mean clique clustering (MCC) (**Figure 7C**). This resulted in 10 MCC hubs, 9 of which were part of the primary schizophrenia-susceptibility network and share no edges with each other thereby creating 10 modules (red (higher rank) to yellow (lower rank) MCC Top10 nodes). We visualized the first-degree neighbors of these hub genes and found that each of the hub genes coordinated its own mini network as predicted (**Figure 7D**). Pathway analysis of this network of Hub genes and their first-degree neighbors results in only 1

statistically significantly enriched term – Cell Cycle (KEGG 2021; Adj. p=0.00096). Ontology analyses showed that biological processes underlying this were transcriptional regulation, RNA processing, ribosomal biogenesis, and regulation of protein phosphorylation with RNA-binding proteins statistically overrepresented in this network (**Table S8**).

Discussion

In this study we investigated the consequence of loss of Nrg1 nuclear back signaling. We confirmed that $V_{321}L$ substitution in Nrg1 disrupts its endogenous proteolytic processing by γ-secretase and downstream Nrg1 ICD nuclear signaling (Figure 2A, 2C). The $V_{321}L$ mouse model is appropriate for studying Nrg1 nuclear signaling as well as investigate its connection to schizophrenia disease pathogenesis.

Examination of the MUT DG transcriptome revealed aberrations in genetic programs governing neurogenesis and neuronal maturation (Figure 3C, 3E). Closer experimental examination of neurogenesis in the hippocampal neurogenic niche revealed depletion of the neural stem cell pool and accelerated cell cycle exit. The depletion of the proliferative cell population is not sporadic but biased toward the neuronal postmitotic program (Figure 5). Here, postmitotic program selection itself is compromised as evidenced by the reduction of DG mature neuron marker Calbindin 1 and abnormal dendrite morphology (Figures 3E, 6, 7). Accelerated maturation of neurons in the DG is often coupled with aberrant neuronal development and improper integration into local circuits. For example, downregulation of Disrupted-in-schizophrenia 1 (DISC1) in hippocampal neural progenitors resulted in accelerated dendrite outgrowth, along with abnormal migration, hyperexcitability, and early synapse formation (Duan et al. 2007). Likewise, seizure-induced hippocampal neurogenesis yielded greater numbers of neurons with accelerated dendrite arborization, but the neurons were often ectopically positioned and received aberrant recurrent synaptic inputs (Parent et al. 1997, Overstreet-Wadiche et al. 2006). These aberrations in neuronal production have far-reaching implications for newborn neuron integration into local circuitry.

We found that granule cells from the MUT DG displayed a shift in dendritic mass towards the soma and decreased distal dendrite complexity (Figure 6 C, D, E). This change in dendrite morphology has important implications for functional connectivity of the entorhinal cortex and the DG in the MUT brain. The lateral perforant path supplies the major input into distal dendrites of dentate granule cells and relays information about local cues and context (Amaral et al. 2007, Luna et al. 2019). Disruptions to this circuitry have important repercussions for contextual learning and disease relevance to schizophrenia and psychosis. One possible mechanism for the loss in granule cell dendrite complexity is the observed loss of kinetochore gene expression in MUT DG. Kinetochore gene products are expressed in post-mitotic neurons where they localize to the synaptic neuropil and are likely part of the microtubule organizing centers (MTOCs) that maintain the dendritic cytoskeleton. Loss of function of these genes results in loss of dendritic complexity in cultured neurons (Zhao G., et al. 2019). In line with this, we also note downregulation of *homologous to augmin subunits* (*HAUS*) family genes, which are known to regulate mitotic spindle assembly (Lawo S., et al. 2009) but regulate axon and dendrite development in neurons (Cunha-Ferreira I., et al. 2018). Neurons face a unique challenge of having to establish MTOCs far away from the cell body for appropriate branching of the dendritic arbor to receive

incoming axonal input during early synaptogenesis and this process could be compromised in the mutant DG.

Our finding that Nrg1 nuclear signaling downstream of gamma-secretase processing is necessary for dendrite outgrowth but not axon outgrowth in culture cortical neurons is consistent with the hypothesis of two independent modes of Nrg1 back-signaling. Previous work has shown that ErbB4 ligand binding to the EGF-like domain of Nrg1 can initiate local PI3K-dependent signaling in central and peripheral axons and that it can also induce cleavage of the NRG1 ICD, leading to ICD nuclear translocation (Bao J., et al 2003; Hancock M., et al. 2008). Type III Nrg1 KO neurons show both axonal and dendritic growth defects, which can be rescued by re-expression of the protein (Chen Y., et al. 2010). Gamma-secretase cleavage of Type III Nrg1 is necessary for normal dendrite growth but is dispensable for axonal growth (**Figure S6-2**) and Chen Y., et al. 2010). Overexpression of the NRG1 ICD increases dendritic growth and complexity of cultured hippocampal neurons, an effect not observed by overexpression of the ICD lacking a nuclear localization sequence (Fazzari P., et al. 2014). Taken together, our results show that, with respect to neurite outgrowth, Nrg1-PI3K and Nrg1 nuclear back-signaling appear to operate in mutually exclusive, independent pathways.

Dysregulation of polycomb repressor activity as a predicted mechanism for ectopic gene expression and precocious differentiation in the MUT DG.

We found that over half of the upregulated genes in the mutant DG were predicted targets for the polycomb repressor complex 2 (PRC2 – Suz12, Ezh2) and that expression of *eed* and *ezh2*, catalytic subunits of the PRC, was reduced in the MUT DG (Figure S3A and Table S1). PRC mediated repression is critical for maintaining self-renewal of stem cells and preventing differentiation (Sparmann A. & van Lohuizen M. 2006; Boyer LA., et al. 2006). Many genes associated with neuronal differentiation are bound by PRC2 in proliferating cells which experience a depletion of PRC2 upon treatments that promote neuronal fate commitment (e.g., retinoic acid) (Bracken AP., et al. 2006). We noted that genes involved in suppression of proliferation and/or promoting neuronal differentiation (*ptpru, nell1, bmp2, sfrp2, igfbp3, igfbp6, sstr4, myo16, zbtb7c*) were upregulated (Table S2).

$V_{321}L$ mutation in Nrg1 disrupts a schizophrenia-susceptibility gene network.

Genetic variants that influence gene expression, eQTLs, are thought to comprise a significant proportion of genetic risk in schizophrenia (Richards AL., et al. 2012). The cellular mechanisms by which these changes in gene expression influence risk for schizophrenia are not clear. We found a significant enrichment of genes associated with psychotic disorders to be dysregulated in the MUT DG (Figure 3D; Figure 7A). We examined known interaction networks between these genes and found several modular hubs with hub genes represented by the known schizophrenia-associated genes. Pathway analysis showed that genes interacting with the schizophrenia-susceptibility genes are enriched for physiological processes and pathways known to be associated with schizophrenia such as glutamatergic/dopaminergic synaptic transmission, nicotine addiction, or Akt signaling. The hub gene network (hub genes+1st degree neighbors) within this expanded schizophrenia-susceptibility gene network showed a much more specialized functional enrichment of genes involved in regulation of cell cycle, which is a DG-specific feature in the hippocampus owing to the presence of proliferating stem cells. These data highlight the need to examine cell-type specific eQTL signatures and their regulation to better grasp mechanisms underlying the pathology within a given brain region or circuit.

Conclusions

In this study we demonstrate that the Val→Leu mutation in Nrg1 results in disruption of Nrg1 nuclear back signaling and transcriptional regulation in the DG. Transcriptomic changes in the MUT

DG were found to be associated with dysregulation of proliferation, differentiation, and dendrite outgrowth. Our findings are consistent with these predictions showing that MUT mice indeed have reduced stem cell proliferation and altered cell cycle dynamics resulting in precocious neuronal differentiation in the DG. Further, we found that granule cells in the MUT DG show aberrant development of dendrites throughout their maturation. Transcriptomic changes in the MUT DG were found to be enriched for genes whose human orthologs are associated with schizophrenia and related neurodevelopmental disorders.

Ideas & Speculations

ErbB4 binding to Nrg1 can act as a signal to generate nuclear ICD clusters and requires functional gamma secretase to do so (Figure 2). In neurons, Type III Nrg1 is a synaptic protein, as is its receptor ErbB4. In the mouse hippocampus, ErbB4 expression is mostly accounted for by different subtypes of interneurons in the DG (Neddens and Buananno 2010), which are some of the first synaptic partners of newborn dentate granule cells, providing input early during granule cell maturation (Ge S., et al. 2006). Additionally, granule cells strongly innervate GABAergic neurons in the CA3, which are known to express ErbB4 (Vullhorst D., et al. 2009; Acsady L., et al. 1998). Thus, ErbB4+ GABAergic axon terminals could provide the signal to early maturing neurons by stimulating somato-dendritic Nrg1 at GABAergic postsynaptic sites, and/or axonal Nrg1 could potentially be retrogradely trafficked to the nucleus after interaction with CA3 interneuron dendrites. While the spatio-temporal regulation of Nrg1 back signaling is not clear, in the hippocampus, ErbB4 expression is predominantly present at postsynaptic sites (Vullhorst D., et al. 2009). Thus, we propose that ErbB4-regulated nuclear back-signaling might originate at dentate granule cell axonal pre-synapses. We hypothesize that in neurons, the Nrg1 ICD coordinates changes in gene expression as a function of synaptogenic interactions. Mechanistically, this change in gene expression might serve to establish a genomic landscape that signals the dendrites to mature, accept afferents and integrate into a circuit as the axons form synapses on the efferent end. It is also possible that the effect of the nuclear ICD is dependent upon developmental stage-specific chromatin landscape such that nuclear back-signaling originating from early afferent synaptogenesis from GABAergic neurons regulates a different set of genes than those regulated by efferent synaptogenesis.

How does the ICD regulate gene expression? The Nrg1 ICD has been shown to physically interact with a core subunit (Baf57) and the catalytic ATPase (Smarca2) of a BAF chromatin remodeling complex (SWI/SNF) in cultured neural stem cells (Pirotte D., et al. 2010). In this study we found evidence hinting at dysregulation of the polycomb repressor complex (PRC) in $V_{321}L$ mutant DG. A few studies have proposed antagonism between these two gene regulatory complexes such that SWI/SNF complex can suppress expression of PRC genes, and directly evict PRC from its target genes (Kadoch C., et al, 2016). This raises the intriguing possibility that the Nrg1 ICD's interaction with the key catalytic ATPase subunit of a BAF complex might potentially serve to inactivate it, and/or alter its genomic targeting. In this manner, a stimulus-specific regulated dose of nuclear ICD protein could lead to stimulus/cell state-specific function of the PRC leading to a balance between self-renewal and differentiation in stem cells. In the case of differentiating or maturing neurons, this could potentially be a mechanism by which a neuron's genome can sense efferent synaptogenesis and initiate gene expression necessary for completion of afferent synaptogenesis.

Our data demonstrate that introduction of the schizophrenia-associated $V_{321}L$ mutation in Nrg1 resulted in dysregulation of orthologs of known schizophrenia-susceptibility genes in the mutant DG. Thus, it's possible that individual eQTLs don't contribute to risk independently but instead as a functional gene regulatory network underlying their association with the disease. In this case we hypothesize that synaptogenic interactions (in the form of the nuclear ICD) regulate this network of

genes. This supports a mechanistic framework to understand the growing idea that schizophrenia-associated rare and common genetic variants result in convergent dysregulation of glutamatergic synaptogenesis. Along these lines, it might also be possible that environmental risk for schizophrenia involves disruption of synaptogenic processes resulting in a convergent transcriptomic dysregulation not necessitating the presence of these eQTLs.

We propose that Nrg1 ICD might be one regulator that communicates synaptogenesis to the genome in excitatory projection neurons. However, there are numerous other regulators that are related to genetic and environmental risk factors such as Creb mediating activity-dependent transcription or Esr/Ar mediating gonadal hormone-induced gene expression. The stimuli activating these regulators are serially arranged along a neurodevelopmental continuum – axonal target innervation, excitatory postsynaptic activity, pubertal hormone surges. Understanding whether the gene regulatory landscapes between these regulators/stimuli interact and what mechanisms underlie such interactions might be crucial in understanding the complex etiology of schizophrenia.

Methods & Materials

KEY RESOURCES TABLE

REAGENT or RESOURCE	SOURCE	IDENTIFIER
Antibodies		
Rabbit anti-Neuregulin1 B1a (1:500)	Santa Cruz	Cat# sc-348 Lot# D2816, H0403, G122
Raw sequencing reads	This paper	SRA accession code
Mouse anti-Neuregulin1 CRD (1:100)	NeuroMab	Cat# 75-226 Lot# 447 Clone N126B/31
BenchStable DMEM	Gibco	Cat# A4192101
Glutamax	Gibco	Cat# 35050061
Rabbit- Neuregulin1 B1a (ICC-1:500, WB-1:1000)	This paper	N/A
Rabbit- Prox1 (1:1000)	Abcam	Cat# ab101851
Mouse anti-TuJ (1:1000)	Biolegend/Covance	Cat# MMS-435P
Rabbit anti-Ki67 (1:500)	Abcam	Cat# ab15580 Lot# GR257727-1, GR300154-1
Goat anti-Dcx (1:500)	Santa Cruz	Cat# sc-8066 Lot# K1215
Rabbit anti-GFP (1:1000)	LifeTech	Cat# A11122 Lot# 1828014
IRDye800-conjugated Affinity Purified Goat anti-Rabbit IgG (H&L) (1:20,000)	Rockland	Cat# 611-132-002 Lot# 23205
Goat anti-Rabbit Alexa Fluor 680 conjugate (1:30,000)	LifeTech	Cat# A21109 Lot# 433580
Donkey anti-Rabbit Alexa Fluor 488 conjugate (1:1000)	LifeTech	Cat# A21206 Lot# 1910751
Donkey anti-Rabbit Alexa Fluor 594 conjugate (1:1000)	LifeTech	Cat# A21207 Lot# 1668652
Donkey anti-Goat Alexa Fluor 488 conjugate (1:1000)	LifeTech	Cat# A11055 Lot# 412435

Donkey anti-Mouse Alexa Fluor 488 (1:1000)	LifeTech	Cat# A21202 Lot# 41225A, 1796361
Bacterial and Virus Strains		
MMLV (VSV-G)-GFP	Dr.Shaoyu Ge	https://www.nature.com/articles/nature04404
Chemicals, Peptides, and Recombinant Proteins		
Recombinant Mouse ErbB4/Her4 Fc Chimera Protein, CF	R&D Systems	Cat# 4387-ER-050
Papain from papaya latex	Sigma	Cat# P4762 Lot# SLBZ8588
BDNF	Gibco	Cat# 10908-010
B-27™ Supplement (50X), serum free	Gibco	Cat# 17504044
Paraformaldehyde, 32% w/v aq. soln., methanol free	Thermo Scientific	Cat# 473779M
DAPI Fluoromount G	Southern Biotech	Cat# 101442-494
Spectral DAPI	Akoya Biosciences	Cat# FP1490
Prolong Gold Antifade	ThermoFisher	Cat# P36934
cOmplete™ Protease Inhibitor Cocktail	Sigma Aldrich	Cat# 11836145001
PhosSTOP™	Sigma Aldrich	Cat# 4906837001
DAPT	CST	Cat# 15020S
RNA*later*™ Stabilization Solution	Invitrogen	Cat# AM7020
Hibernate-A medium	Gibco	Cat# A1247501
Opal 570 Reagent Pack	Akoya Biosciences	Cat# FP1488001KT
Opal 620 Reagent Pack	Akoya Biosciences	Cat# FP1495001KT
Opal 690 Reagent Pack	Akoya Biosciences	Cat# FP1497001KT
Deposited Data		
RNA-Seq data	https://www.ncbi.nlm.nih.gov/geo/query/acc.cgi?acc=GSE192869	GEO Accession code: GSE192869
Experimental Models: Cell Lines		
Neuro-2a (ATCC® CCL-131™)	ATCC	
HEK293-T	ATCC	
Experimental Models: Organisms/Strains		
Mouse: V321L: Nrg1tm1Dat V/L	This paper	
Oligonucleotides		
Genotyping Fwd Primer: 5'-GGTGATCCCATACCCAAGACTCAG-3'	IDT	
Genotyping Rev Primer: 5'-CTGCACATTTATAGAGCATTTATTTTG -3'	IDT	
Type III Nrg1 RNAScope probe: a 19ZZ probe named **Mm-Nrg1-O5** targeting 34-1171 of NM_001364422	ACD/Bio-Techne	This study (custom probe)
Recombinant DNA		
pUX-GFP	Dr.Shaoyu Ge	

pCMV-VSV-G	Dr.Shaoyu Ge	Addgene Plasmid #8454
GP	Dr.Shaoyu Ge	
TypeIII Nrg1-YFP	Dr. Kevin Czaplinski	
Software and Algorithms		
Code for RNASeq analysis	https://github.com/RajNINDS/V321L_DG	

Experimental model and subject details
Male and female mice ages E18.5 - 6 months were used. Animals were housed in a 12-hour light/dark cycle environment that was both temperature and humidity controlled. Animals had free access to food and water. All animal care and experimental procedures were approved by the Institutional Animal Care and Use Committee of the SUNY Research Foundation at Stony Brook University, Stony Brook NY and NINDS, National Institutes of Health, Bethesda MD.

Genotyping
Genotypes were determined by PCR using the following primers:
Forward primer 5'- GGTGATCCCATACCCAAGACTCAG -3'
Reverse primer 5'- CTGCACATTTATAGAGCATTTATTTTG -3'

Antibody generation
Antibodies recognizing the NRG1 intracellular domain were raised in rabbits using the immunizing peptide: DEE(pY)ETTQEYEPAQEP by Biomatik. Antibodies recognizing the phosphorylated peptide DEE(pY)ETTQEYEPAQEP vs. the unphosphorylated peptide DEEYETTQEYEPAQEP were purified by affinity chromatography.

Nuclear fractionation
For each experiment, cortex, and hippocampus were pooled by genotype for nuclear fractionation. P86-108 animals were deeply anesthetized with isofluorane and decapitated, and cortex and hippocampus were isolated on ice and homogenized with Dounce homogenizer on ice in 5mL nuclear fractionation buffer (60mM KCl, 15mM NaCl, 15mM Tris-HCl pH7.6, 1mM EDTA, 0.2mM EGTA, 15mM 2-mercaptoethanol, 0.5mM spermidine, 0.15 spermine, 0.32M sucrose, cOmplete ULTRA tablets protease inhibitor cocktail). Samples were first homogenized with the loose pestle checking for single, dispersed cells after every 10 strokes using a hemocytometer. Samples were then homogenized with the tight pestle checking for dissociated nuclei after every 10 strokes. Samples were centrifuged at 1000 *xg* for 10 minutes at 4°C. Pellets were resuspended in nuclear fractionation buffer with 0.1% Triton X-100 and incubated on ice for 10 minutes and then pelleted at 1000 *xg* for 10 minutes at 4°C. Pellets were resuspended in 500µL nuclear fractionation buffer, layered over 500µL of a 1M sucrose (in nuclear fractionation buffer) cushion, and centrifuged at 1000 *xg* for 10 minutes at 4°C. Pellets were resuspended in 1mL nuclear fractionation buffer. Laemmli buffer was added to each sample and boiled at 95°C for 5 minutes. Denatured samples were stored overnight at -20°C. Protein analysis was then performed by immunoblot.

Immunoblotting
Samples were electrophoresed on 8% SDS-PAGE gel at 90V for 1.5 hours at room temperature. Proteins were transferred onto nitrocellulose membranes via wet transfer performed at 4°C at 100V for 1 hour. Membranes were blocked in Odyssey Blocking Buffer (LI-COR #927-40000) for 1 hour at room temperature with gentle agitation. Membranes were then incubated overnight on a rocker at 4°C with primary antibodies diluted in 50% blocking buffer. The next day, membranes were washed 3 times with PBS-T (PBS+0.1% Tween20) and incubated with secondary antibodies (diluted in 50% blocking buffer) for 1 hour at room temperature with gentle agitation. After 3 washes in PBS-T,

membranes were imaged using the LI-COR Odyssey Infrared Imaging System. Protein signals were then quantified using ImageJ as average grey value in each band.

Cell culture:

Primary neuronal culture:

PND4 or E18.5 WT (VV) and MUT (LL) mice were rapidly decapitated, and their brains were transferred to ice-cold Hibernate-A. Hippocampi/cortices were dissected out and transferred to Hibernate-A (ThermoFisher Cat# A1247501) on ice. Hibernate solution was removed and replaced with activated and filtered Papain (Sigma Cat# P4762, Lot# SLBZ8588) dissolved in Hibernate-A. Hippocampi were digested for 15min in a 37ºC water bath gently inverting the tube every 5min. Papain solution was removed, and digested tissue was washed thoroughly (4x) with wash solution (Hibernate-A+10%FBS+100U DNase I (StemCellTech. Cat#07469)) by resuspending the tissue in wash solution and allowing it to settle before replacing wash solution. 40µm cell strainers were placed over 50mL conical tubes and wet with plating medium (Neurobasal+B27+Glutamax+Pen/Strep+HEPES) and flowthrough was discarded. Wide and narrow bore fire-polished Pasteur pipettes were pre-wet with FBS and were used to triturate the tissue into a single-cell suspension. The cell-suspension was applied to the pre-wet cell strainer and flow through was collected and analyzed for live/dead cells using Trypan blue on the CountessII automated cell counter. Appropriate number of cells were plated into 24 well plates containing 12mm Poly-D-Lysine+Laminin coated coverslips in a total volume of 250µL/well. Neurons were left overnight to adhere, and 250µL fresh plating medium was added the following day to each well. 50% of the total media was replaced every other day until experimental time points.

Cell line culture and transfection:

Neuro2A cells (ATCC) were maintained in DMEM+10%FBS+1:1000 Gentamycin.
Cells were passaged on a Mon-Wed-Fri scheduled and were not used beyond 10 passages. Cells were transfected with plasmid DNA using Lipofectamine2000 following manufacturer guidelines. Plasmid details can be found in the Key Resources Table.

Stimulation & drug treatments:

Recombinant Mouse ErbB4/Her4 Fc Chimera Protein was reconstituted at a final concentration of 0.5µM and stored at -80ºC. Working stocks of 0.1µM were prepared and stored briefly at -20ºC. For stimulation experiments, 20nM ErbB4 solution was prepared by diluting 0.1µM stock solution in 125µL Neurobasal plating medium/well.
Neurons were washed by gently swirling the plate and aspirating out all the media and near-simultaneously replacing with 125µL of fresh pre-warmed plating media and equal volume of ErbB4 solution was added to obtain a final concentration of 10nM.
For imaging nuclear ICD, neurons were stimulated for 20min and for axonal/dendritic growth experiments stimulation was done for 4 hours.
Drug concentrations, (pre)treatment periods are listed in the table below:

Drug Name	Maufacturer	Concentration	Pre-Treatment Time
DAPT	CST	20 µM	24h
Wortmannin	Sigma	500 nM	45 min
L-685,458	Sigma	5 µM	45 min

Immunocytochemistry:

Neurons were fixed for 5min at room temperature (RT) in 4% PFA by adding equal volume of 8%PFA to neurobasal in the wells. Entire solution was replaced with fresh 4%PFA and neurons were fixed further for 10min at RT. Coverslips were washed 3x 5min each in 1xPBS-G (PBS+0.1M Glycine), incubating in the final wash for 10min. Neurons were then permeabilized in 0.1% Triton X-100 in 1xPBS for 15min at RT. Coverslips were washed 3x 5min each with 1x PBS-G and incubated in

blocking solution (10% normal donkey serum-NDS) for 30min. After blocking, coverslips were incubated with primary antibodies prepared in 1% NDS overnight at 4ºC. Coverslips were washed thoroughly with 1xPBS at RT 3x 5min each and were then incubated with secondary antibodies prepared in 1%NDS+0.1%Triton X-100. Coverslips were washed thoroughly with 1xPBS at RT 3x 5min each and mounted in mounting medium containing DAPI (DAPI Fluoromount-G™ - Southern Biotech). Antibodies used and concentrations can be found in the Key Resources Table (KRT).

Tissue processing and immunohistochemistry:
Animals were deeply anesthetized with isofluorane and transcardially perfused with 4% paraformaldehyde (PFA) in PBS. Brains were harvested and post-fixed overnight at 4°C in 4% PFA in PBS. Brains were transferred to 30% sucrose in PBS and incubated at 4°C with agitation until they sank. Brains were embedded in optimal cutting temperature (O.C.T.) compound, flash frozen and stored at -80°C. 20-50µm sections were obtained serially over the entire dorsoventral extent of the hippocampus, and each slide collected 1 of every 8 (20 µm) or 1 of every 4 sections (50 µm). Sections were dried at room temperature overnight prior to immunohistochemistry.
Antigen retrieval was performed by immersing sections in antigen retrieval buffer (10mM sodium citrate, 0.05% Tween20, pH 6.0) at 100°C for 15 minutes. Sections were then allowed to cool to room temperature and neutralized in 0.1M borate buffer, pH8.5 for 10 minutes at room temperature. After 3 5-minute washes in PBS, sections were incubated in blocking buffer (5% normal donkey serum, 0.1% Triton X-100 in PBS) for 1 hour at room temperature. Sections were then incubated with primary antibodies diluted in blocking buffer for 48 hours at 4°C in a humidity chamber. After 3 5-minute washes in PBS, sections were then incubated with secondary antibodies diluted in blocking buffer for 1 hour at room temperature. Sections were dehydrated in 70% ethanol for 5 minutes and treated with autofluorescence eliminator reagent (Millipore Sigma 2160). No. 1.5 glass coverslips were then mounted on the slides with DAPI Fluoromount-G and allowed to dry overnight at room temperature. Antibodies used and concentrations can be found in the Key Resources Table (KRT).

Fluorescent in-situ hybridization (FISH):
Brains were fixed and cryosectioned as described earlier. 25um sections were prepared with one coronal section on a slide containing the dorsal hippocampus. FISH was performed per manufacturer's instructions using the RNAscope v2 fluorescent multiplex assay (ACD/Bio-Techne, CA). Details on the probe used to target the TypeIII Nrg1 transcript can be found in the KRT.

Imaging & image analysis:
To image NRG1 ICD puncta in the nucleus, imaging was done on the Zeiss LSM800 confocal microscope using the 63x oil immersion objective. All samples were imaged using identical parameters. Neurons to analyze were identified by expression of TYPE III NRG1 (CRD+), and their nuclei were imaged at 2.5x digital zoom with 1µm z-steps.
Image processing and analysis was performed using ImageJ (FIJI). Briefly, center of the nucleus was identified and 1 z-section above and below it was flattened via maximum intensity projection. DAPI-stained nuclei were outlined, and the enclosed area was measured and noted. ICD clusters were manually counted using the cell-counter plugin. Density of clusters was calculated by dividing number of clusters by the nuclear area.
Images examining Type III Nrg1 expression profile in the dentate gyrus and images used for Ki67+ and doublecortin+ cell density counts were acquired on Olympus FLV1000 confocal microscope at 20X magnification with 3-µm z-steps. Images were analyzed in ImageJ using the Cell Counter plugin. Only cells located in the subgranular zone of the dentate gyrus was counted. Total cell counts for each animal were divided by the total dentate gyrus volume counted to obtain cell density. For each animal, 12-14 coronal sections were sampled along the entire dorsoventral extent of the dentate gyrus.
EdU labeling counts were done on images acquired using Olympus VS-120 microscope at 20X magnification. Images were acquired at 1-µm Z-steps of the entire dentate gyrus hemisection. Images

were analyzed in ImageJ using the Cell Counter plugin. Total cell counts for each animal were divided by the total dentate gyrus volume counted to obtain cell density. For each animal, 12-14 coronal sections were sampled along the entire dorsoventral extent of the dentate gyrus.
Ki67+ total cell counts in P21 animals were done using the Optical Fractionator probe on the Stereo Investigator software (MBF Bioscience) coupled to live imaging on an epifluorescent microscope. Section sampling fraction was 1 every 8th section, counting frame size used was 100 µm x 100 µm, and guard zone height used was 10 µm. All sample counts achieved a Gundersen coefficient of error of <0.1.

Golgi impregnation, sampling criteria, imaging, & analysis
P60 animals were deeply anesthetized with isofluorane, and brain samples were harvested quickly on ice and rinsed with ice-cold PBS. The brain samples were then treated with the FD Rapid GolgiStainTM Kit (FD NeuroTechnologies, Inc., catalog # PK401) per manufacturer's guidelines. 100 µm brain sections were collected using a vibratome and dried overnight in the dark at room temperature. Sections were then dehydrated in progressively increasing concentrations of ethanol solution (50% → 75% → 95%), then xylene, and coverslipped with Permount solution.
Imaging of Golgi impregnated neurons in the dentate gyrus was done on the Olympus VS-120 microscope at 60x magnification. Individual neurons were selected for imaging based on the following criteria: 1) the neuron's cell body resided in the granule cell layer in the intermediate section of the superior blade, 2) the soma morphology assumed the typical granule cell "tear drop" morphology, 3) the dendritic arbor originated from a single primary dendrite and assumed a cone-shaped morphology 4) the dendritic arbor was not obstructed by other cell bodies or dendrites. 11 neurons from 5 wildtype animals and 13 neurons from 5 homozygous mutants were ultimately selected for analysis. Dendritic arbor tracings, sholl analysis, and branching analysis were done on the NeuronStudio software.

GFP-expressing retrovirus production, injection, imaging, & analysis
GFP-retrovirus was prepared by co-transfection of pUX-GFP, VSVG, and GP constructs (kindly provided by the laboratory of Shaoyu Ge; previously described in (Ge et al. 2006)) into HEK293 cells. Viral supernatant was collected, the retrovirus was concentrated by ultracentrifugation, and the viral pellet resuspended in sterile PBS.
Following anesthetization, ~P90 animals were stereotaxically injected bilaterally in dorsal dentate gyrus (-2.0 mm A/P, +1.6 mm M/L, -2.5 mm D/V) and ventral dentate gyrus (-3.0 mm A/P, +2.6 mm M/L, -3.2 mm D/V). The injection volume was 0.25 µL/site. Following surgery, animals were administered 0.03 mL ketorolac (3 mg/mL) for every 10g body weight.
14 days following stereotaxic viral injections, animals were sacrificed, and brain samples harvested as described previously for tissue preparation. 50-µm floating coronal sections were obtained, and each set of sections contained 1 every 6th section of the hippocampus along its dorsoventral extent. Analysis was done in real time while imaging on the Zeiss Axio Imager A1 Fluorescent Microscope using a 40x oil immersion objective lens. The identity of GFP+ cells were determined by a combination of morphology, Dcx immunoreactivity, and Nissl staining. Neural progenitors were identified by short, tangential processes and the lack of radially oriented processes, with or without Dcx immunoreactivity. Immature granule cells were identified by their radially oriented neurites, Dcx+ and Nissl+ staining. Astrocytes were identified by their star-like morphology, extensive branch ramifications, and lack of Dcx immunoreactivity and Nissl staining.

EdU labeling and tissue processing (cell cycle exit, length, and survival)
To measure cell cycle reentry, EdU (50 µg/g body weight) was injected intraperitoneally in animals at ~P90. 24 hours after EdU injection, animals were sacrificed, and brain samples were harvested and prepared as described in the previous section. To visualize EdU incorporation, the Click-iTTM EdU Cell Proliferation Kit (Thermo Fisher Scientific, catalog # C10338) was used according to manufacturer's guidelines, followed by immunohistochemistry as described in the previous section.

To measure cell cycle length, EdU (50 µg/g body weight) was injected intraperitoneally in animals at P21-30. 30 minutes after EdU injection, animals were sacrificed, and brain samples were harvested and prepared as described in the cell cycle reentry experiment. To measure newborn cell survival, three pulses of EdU (50 µg/g body weight) spaced 24-hours apart were injected intraperitoneally in animals at ~P90. Animals were sacrificed 30 days later, and brain samples harvested

RNA sample prep and sequencing:

All tools, glassware, gloves, and surfaces were cleaned with ethanol and RNaseZAP™(Invitrogen) according to manufacturer guidelines.

Mice were anesthetized using isoflurane (~2min). Mice were then placed in a shallow ice trough and rapidly perfused with 10mL ice-cold 1x phosphate buffered saline (PBS) for a total of 5 min. The brain was immediately removed and transferred to a pre-chilled stainless-steel adult mouse brain matrix placed in ice to make 0.3mm coronal sections (~2min) using pre-chilled blades. The sections were immediately transferred to ice-cold Hibernate-A in a pre-chilled glass petri dish on ice. Dentate gyrus (DG) was visually identified and dissected out from hippocampal sections to isolate the upper and lower blades along with adjoining regions of the hilus and part of the molecular layer (See Figure 3A). The microdissections took no more than 3min per brain. Dissected DG bits were transferred to 1mL RNALater in a microcentrifuge tube placed in ice and were left rotating at 4ºC overnight. The following day, tissue was extracted from RNALater solution, flash frozen using dry ice and 100% ethanol and stored at -80ºC until RNA extraction.

RNA was extracted from flash frozen DG bits using the RNeasy Micro Kit (Qiagen) with on-column DNAse treatment following manufacturer guidelines. RNA was poly-A selected and RNA-Seq libraries were prepared using NEBNext Library Prep Kit for Illumina (NEB #E7760). A Miseq shallow sequencing run was performed after library preparation to balance the sample loading process on the deep sequencer. Sequencing was performed using NSQ 500/550 Hi Output KT v2.5 (150 CYS) (Illumina) to obtain 75bp paired end reads. The estimated read depth was ~33.33 million reads/DG sample.

Differential Gene Expression (DEG) Analysis:

QC inspection was performed on sequencing data using a combination of FastQC, MultiQC, and Fastx_Screen. Next, adaptor sequences were clipped and low quality and/or nucleotide biased positions in sequences were trimmed using the Trimmomatic; QC inspection of the post clipped and trimmed sequences was repeated. Clipped and trimmed sequences were aligned to the mouse reference genome (mm10) using the HISAT2 tool and QC inspection of the alignments was performed using the RSeqC. Transcript assembly was performed using StringTie which included the discovery of any novel genes:isoforms. QC inspection of the assembly was performed using the gffcompare tool. To enumerate both gene-level and transcript-level expression from the assembly output, IsoformSwitchAnalyzeR package supported in R was used. For differential analysis of the enumerated gene-level expression, commands and functions supported in R were used. Briefly, expression per sample was first within sample normalized via cpm (counts per million) then pedestalled by 2 by taking the log2 transformation. To correct for differences in spread and location, required before testing, cross-sample normalization was performed using Cyclic Lowess. Expression after normalization was inspected by cov-based PCA scatterplot to identify any outliers. Using this 1 sample was identified as an outlier (WT female). This sample was further inspected for coverage using a set of house-keeping genes in mm10 and was found to be 5' degraded and as such was excluded from further analysis. Other samples were reinspected for coverage and were found to pass QC. Normalization for the gene-level expression was repeated after outlier removal, and sequence batch was globally corrected for via the Limma tool. Using the noise model plot generated from

Limma, we identified a mean batch-corrected normalized expression value of 2.25 that was then used to filter genes and transcripts not having at least one sample greater than this value while also flooring values to 2.25 for surviving genes and transcripts if less than this value. These filter-floored values for surviving transcripts were tested for differential expression between WT and MUT samples via ANCOVA controlling for sequence batch and biological sex. Dysregulated genes were identified as those having a p-value of <0.05 or <0.1 (colored differently on volcano plot) corrected for batch and/or sex and a minimum fold-change of 1.25 in either direction. Dysregulated genes were then used to perform enrichment analyses using Ingenuity Pathway Analysis (IPA) (Qiagen) and Enrichr (Chen EY., et al. 2013; Kuleshov MV., et al. 2016; Xie Z., et al. 2021).

Statistical analysis
Statistical analysis was performed using Prism (GraphPad). Normality was assessed using Shapiro-Wilkins and Kolmogorov-Smirnov tests. If data failed either test, non-parametric stats were used. p-values were corrected for multiple comparisons as necessary using Bonferroni (parametric) post-hoc test.
For Sholl analysis we followed published guidelines to avoid faulty inferences in Sholl analyses (Wilson MD., et al. 2017). Sholl analysis data did not pass Shapiro-Wilkins normality test; however, given that measurements were made from multiple neurons from the same animal pooled with neurons across animals, we could not use the Wilcoxon rank sum test given the assumption of independence of variables. To address this case, we transformed the data by taking the square-root of the measurements and used a repeated measures two-way ANOVA with a mixed effects model. To control for false discovery rate (FDR) and Type I error inflation, p-values were corrected for multiple comparisons using the original Benjamini-Hochberg FDR procedure.

Resource availability

Lead Contact
Further information and requests for resources and reagents should be directed to and will be fulfilled by Lead Contact, Dr. David Talmage (david.talmage@nih.gov).

Materials Availability
Plasmids used in this study have been deposited to Addgene and will be available upon publication under Talmage Lab.

Data and Code Availability
The data generated in this publication have been deposited in NCBI's Gene Expression Omnibus (Edgar et al., 2002) and are accessible through GEO Series accession number GSE192869 (https://www.ncbi.nlm.nih.gov/geo/query/acc.cgi?acc=GSE192869).

Code is available at https://github.com/RajNINDS/V321L_DG

Acknowledgements

This work was supported by MH087473 to DAT as well as the Intramural Research Program of NINDS. We would like to thank Dr. Shaoyu Ge (Stony Brook University, NY) for providing reagents. We would also like to thank Dr. Abdel Elkahloun (NHGRI sequencing core facility) for providing NGS consultation

and services. In additional we would like to thank Wendy Akmentin, Dr. Mala Ananth, and Li Bai for expert technical assistance in data curation.

Disclosures

The authors have no conflicts of interest to declare.

References

Acsady, L., Kamondi, A., Sık, A., Freund, T., & Buzsáki, G. (1998). GABAergic cells are the major postsynaptic targets of mossy fibers in the rat hippocampus. *Journal of neuroscience*, *18*(9), 3386-3403.

Alaerts, M., Ceulemans, S., Forero, D., Moens, L. N., De Zutter, S., Heyrman, L., ... & Del-Favero, J. (2009). Support for NRG1 as a susceptibility factor for schizophrenia in a northern Swedish isolated population. *Archives of general psychiatry*, *66*(8), 828-837.

Altman, J., & Das, G. D. (1965). Autoradiographic and histological evidence of postnatal hippocampal neurogenesis in rats. *Journal of Comparative Neurology*, *124*(3), 319-335.
Amaral, D. G., Scharfman, H. E., & Lavenex, P. (2007). The dentate gyrus: fundamental neuroanatomical organization (dentate gyrus for dummies). *Progress in brain research*, *163*, 3-790.

Bao, J., Wolpowitz, D., Role, L. W., & Talmage, D. A. (2003). Back signaling by the Nrg-1 intracellular domain. *The Journal of cell biology*, *161*(6), 1133-1141.
Bao, J., Lin, H., Ouyang, Y., Lei, D., Osman, A., Kim, T. W., ... & Ambron, R. T. (2004). Activity-dependent transcription regulation of PSD-95 by neuregulin-1 and Eos. *Nature neuroscience*, *7*(11), 1250-1258.

Bond, A. M., Ming, G. L., & Song, H. (2015). Adult mammalian neural stem cells and neurogenesis: five decades later. *Cell stem cell*, *17*(4), 385-395.

Boyer, L. A., Plath, K., Zeitlinger, J., Brambrink, T., Medeiros, L. A., Lee, T. I., ... & Jaenisch, R. (2006). Polycomb complexes repress developmental regulators in murine embryonic stem cells. *nature*, *441*(7091), 349-353.

Bracken, A. P., Dietrich, N., Pasini, D., Hansen, K. H., & Helin, K. (2006). Genome-wide mapping of Polycomb target genes unravels their roles in cell fate transitions. *Genes & development*, *20*(9), 1123-1136.

Chen, E. Y., Tan, C. M., Kou, Y., Duan, Q., Wang, Z., Meirelles, G. V., ... & Ma'ayan, A. (2013). Enrichr: interactive and collaborative HTML5 gene list enrichment analysis tool. *BMC bioinformatics*, *14*(1), 1-14.

Chen, Y., Hancock, M. L., Role, L. W., & Talmage, D. A. (2010). Intramembranous valine linked to schizophrenia is required for neuregulin 1 regulation of the morphological development of cortical neurons. *Journal of Neuroscience*, *30*(27), 9199-9208.

Chen, Y., Role, L. W., & Talmage, D. A. (2011). 15. Mutant Models of Nrg1 and ErbB4: Abnormalities of Brain Structures, Functions, and Behaviors Relevant to Schizophrenia. In *The Origins of Schizophrenia* (pp. 382-412). Columbia University Press.

Chen, Y. J. J., Johnson, M. A., Lieberman, M. D., Goodchild, R. E., Schobel, S., Lewandowski, N., ... & Role, L. W. (2008). Type III neuregulin-1 is required for normal sensorimotor gating, memory-related behaviors, and corticostriatal circuit components. Journal of Neuroscience, 28(27), 6872-6883.

Cunha-Ferreira, I., Chazeau, A., Buijs, R. R., Stucchi, R., Will, L., Pan, X., ... & Hoogenraad, C. C. (2018). The HAUS complex is a key regulator of non-centrosomal microtubule organization during neuronal development. *Cell reports*, *24*(4), 791-800.

Dejaegere, T., Serneels, L., Schäfer, M. K., Van Biervliet, J., Horré, K., Depboylu, C., ... & De Strooper, B. (2008). Deficiency of Aph1B/C-γ-secretase disturbs Nrg1 cleavage and sensorimotor gating that can be reversed with antipsychotic treatment. *Proceedings of the National Academy of Sciences*, *105*(28), 9775-9780.

Duan, X., Chang, J. H., Ge, S., Faulkner, R. L., Kim, J. Y., Kitabatake, Y., ... & Song, H. (2007). Disrupted-In-Schizophrenia 1 regulates integration of newly generated neurons in the adult brain. *Cell*, *130*(6), 1146-1158.

Edgar, R., Domrachev, M., & Lash, A. E. (2002). Gene Expression Omnibus: NCBI gene expression and hybridization array data repository. *Nucleic acids research*, *30*(1), 207-210.

Exposito-Alonso, D., Osório, C., Bernard, C., Pascual-García, S., Del Pino, I., Marín, O., & Rico, B. (2020). Subcellular sorting of neuregulins controls the assembly of excitatory-inhibitory cortical circuits. *Elife*, *9*, e57000.

Falls, D. L. (2003). Neuregulins: functions, forms, and signaling strategies. *The EGF Receptor Family*, 15-31.

Fazzari, P., Paternain, A. V., Valiente, M., Pla, R., Luján, R., Lloyd, K., ... & Rico, B. (2010). Control of cortical GABA circuitry development by Nrg1 and ErbB4 signalling. *Nature*, *464*(7293), 1376-1380.

Fazzari, P., Snellinx, A., Sabanov, V., Ahmed, T., Serneels, L., Gartner, A., ... & De Strooper, B. (2014). Cell autonomous regulation of hippocampal circuitry via Aph1b-γ-secretase/neuregulin 1 signalling. *Elife*, *3*, e02196.

Fleck, D. (2015). *Regulated intramembrane proteolysis of NRG1 type III dediates postnatal peripheral myelination* (Doctoral dissertation, lmu).

Fleck, D., Voss, M., Brankatschk, B., Giudici, C., Hampel, H., Schwenk, B., ... & Haass, C. (2016). Proteolytic processing of neuregulin 1 type III by three intramembrane-cleaving proteases. *Journal of Biological Chemistry*, *291*(1), 318-333.

Ge, S., Goh, E. L., Sailor, K. A., Kitabatake, Y., Ming, G. L., & Song, H. (2006). GABA regulates synaptic integration of newly generated neurons in the adult brain. *Nature*, *439*(7076), 589-593.

Hancock, M. L., Canetta, S. E., Role, L. W., & Talmage, D. A. (2008). Presynaptic type III neuregulin1-ErbB signaling targets α7 nicotinic acetylcholine receptors to axons. *The Journal of cell biology*, *181*(3), 511-521.

Harrison, P. J., & Law, A. J. (2006). Neuregulin 1 and schizophrenia: genetics, gene expression, and neurobiology. *Biological psychiatry*, *60*(2), 132-140.

Harrison, P. J., & Weinberger, D. R. (2005). Schizophrenia genes, gene expression, and neuropathology: on the matter of their convergence. *Molecular psychiatry*, *10*(1), 40-68.

Lee, S. H., DeCandia, T. R., Ripke, S., Yang, J., Sullivan, P. F., Goddard, M. E., ... & Wray, N. R. (2012). Estimating the proportion of variation in susceptibility to schizophrenia captured by common SNPs. *Nature genetics*, *44*(3), 247-250.

Hu, N., Sun, H., Fu, G., Zhang, W., Xiao, Y., Zhang, L., ... & Lui, S. (2020). Anatomic abnormalities of hippocampal subfields in never-treated and antipsychotic-treated patients with long-term schizophrenia. *European Neuropsychopharmacology*, *35*, 39-48.

Jaffe, A. E., Hoeppner, D. J., Saito, T., Blanpain, L., Ukaigwe, J., Burke, E. E., ... & Hyde, T. M. (2020). Profiling gene expression in the human dentate gyrus granule cell layer reveals insights into schizophrenia and its genetic risk. *Nature neuroscience*, *23*(4), 510-519.

Jahn, H. M., & Bergami, M. (2018). Critical periods regulating the circuit integration of adult-born hippocampal neurons. *Cell and tissue research*, *371*(1), 23-32.

Kadoch, C., Copeland, R. A., & Keilhack, H. (2016). PRC2 and SWI/SNF chromatin remodeling complexes in health and disease. *Biochemistry*, *55*(11), 1600-1614.

Kukshal, P., Bhatia, T., Bhagwat, A. M., Gur, R. E., Gur, R. C., Deshpande, S. N., ... & Thelma, B. K. (2013). Association study of neuregulin-1 gene polymorphisms in a North Indian schizophrenia sample. *Schizophrenia research*, *144*(1-3), 24-30.

Kuleshov, M. V., Jones, M. R., Rouillard, A. D., Fernandez, N. F., Duan, Q., Wang, Z., ... & Ma'ayan, A. (2016). Enrichr: a comprehensive gene set enrichment analysis web server 2016 update. *Nucleic acids research*, *44*(W1), W90-W97.

Lachmann, A., Xu, H., Krishnan, J., Berger, S. I., Mazloom, A. R., & Ma'ayan, A. (2010). ChEA: transcription factor regulation inferred from integrating genome-wide ChIP-X experiments. *Bioinformatics*, *26*(19), 2438-2444.

Lawo, S., Bashkurov, M., Mullin, M., Ferreria, M. G., Kittler, R., Habermann, B., ... & Pelletier, L. (2009). HAUS, the 8-subunit human Augmin complex, regulates centrosome and spindle integrity. *Current biology*, *19*(10), 816-826.

Li, R., Chen, M., Tian, H., Li, G., Wang, L., Tu, W., ... & Li, J. (2020). Association between ErbB4 gene function in synaptogenesis and schizophrenia pathogenesis. *Biotechnology & Biotechnological Equipment*, *34*(1), 135-143.

Luna, V. M., Anacker, C., Burghardt, N. S., Khandaker, H., Andreu, V., Millette, A., ... & Hen, R. (2019). Adult-born hippocampal neurons bidirectionally modulate entorhinal inputs into the dentate gyrus. *Science*, *364*(6440), 578-583.

McClellan, J., & King, M. C. (2010). Genetic heterogeneity in human disease. *Cell*, *141*(2), 210-217.

G. L. Ming and H. Song, “Adult Neurogenesis in the Mammalian Central Nervous System,” Annu Rev Neurosci, Vol. 28, 2005, pp. 223-250.

Nakahara, S., Turner, J. A., Calhoun, V. D., Lim, K. O., Mueller, B., Bustillo, J. R., ... & Van Erp, T. G. (2020). Dentate gyrus volume deficit in schizophrenia. *Psychological medicine*, *50*(8), 1267-1277.

Neddens, J., & Buonanno, A. (2010). Selective populations of hippocampal interneurons express ErbB4 and their number and distribution is altered in ErbB4 knockout mice. *Hippocampus*, *20*(6), 7

Parent, J. M., Timothy, W. Y., Leibowitz, R. T., Geschwind, D. H., Sloviter, R. S., & Lowenstein, D. H. (1997). Dentate granule cell neurogenesis is increased by seizures and contributes to aberrant network reorganization in the adult rat hippocampus. *Journal of Neuroscience*, *17*(10), 3727-3738.

Overstreet-Wadiche, L. S., Bromberg, D. A., Bensen, A. L., & Westbrook, G. L. (2006). Seizures accelerate functional integration of adult-generated granule cells. *Journal of Neuroscience*, *26*(15), 4095-4103.

Pirotte, D., Wislet-Gendebien, S., Cloes, J. M., & Rogister, B. (2010). Neuregulin-1 modulates the differentiation of neural stem cells in vitro trough an interaction with the Swi/Snf complex. *Molecular and Cellular Neuroscience*, *43*(1), 72-80.

Provenzano, F. A., Guo, J., Wall, M. M., Feng, X., Sigmon, H. C., Brucato, G., ... & Small, S. A. (2020). Hippocampal pathology in clinical high-risk patients and the onset of schizophrenia. *Biological psychiatry*, *87*(3), 234-242.

Richards, A. L., Jones, L., Moskvina, V., Kirov, G., Gejman, P. V., Levinson, D. F., ... & O'Donovan, M. C. (2012). Schizophrenia susceptibility alleles are enriched for alleles that affect gene expression in adult human brain. *Molecular psychiatry*, *17*(2), 193-201.

Ripke, S., Walters, J. T., O’Donovan, M. C., & Schizophrenia Working Group of the Psychiatric Genomics Consortium. (2020). Mapping genomic loci prioritises genes and implicates synaptic biology in schizophrenia. *MedRxiv*.

Shiota, S., Tochigi, M., Shimada, H., Ohashi, J., Kasai, K., Kato, N., ... & Sasaki, T. (2008). Association and interaction analyses of NRG1 and ERBB4 genes with schizophrenia in a Japanese population. *Journal of human genetics*, *53*(10), 929-935.

Sparmann, A., & van Lohuizen, M. (2006). Polycomb silencers control cell fate, development and cancer. *Nature Reviews Cancer*, *6*(11), 846-856.

Stefansson, H., Petursson, H., Sigurdsson, E., Steinthorsdottir, V., Bjornsdottir, S., Sigmundsson, T., ... & Stefansson, K. (2002). Neuregulin 1 and susceptibility to schizophrenia. *The American Journal of Human Genetics*, *71*(4), 877-892.
Talmage, D. A. (2008). Mechanisms of neuregulin action. In *Novartis foundation symposium* (Vol. 289, p. 74). NIH Public Access.

Vullhorst, D., Neddens, J., Karavanova, I., Tricoire, L., Petralia, R. S., McBain, C. J., & Buonanno, A. (2009). Selective expression of ErbB4 in interneurons, but not pyramidal cells, of the rodent hippocampus. *Journal of Neuroscience*, *29*(39), 12255-12264.

Vullhorst, D., Ahmad, T., Karavanova, I., Keating, C., & Buonanno, A. (2017). Structural similarities between neuregulin 1–3 isoforms determine their subcellular distribution and signaling mode in central neurons. *Journal of Neuroscience*, *37*(21), 5232-5249.

Walsh, T., McClellan, J. M., McCarthy, S. E., Addington, A. M., Pierce, S. B., Cooper, G. M., ... & Sebat, J. (2008). Rare structural variants disrupt multiple genes in neurodevelopmental pathways in schizophrenia. *science*, *320*(5875), 539-543.

Walss-Bass, C., Liu, W., Lew, D. F., Villegas, R., Montero, P., Dassori, A., ... & Raventos, H. (2006). A novel missense mutation in the transmembrane domain of neuregulin 1 is associated with schizophrenia. *Biological psychiatry*, *60*(6), 548-553.

Walton, N. M., Zhou, Y., Kogan, J. H., Shin, R., Webster, M., Gross, A. K., ... & Matsumoto, M. (2012). Detection of an immature dentate gyrus feature in human schizophrenia/bipolar patients. *Translational psychiatry*, *2*(7), e135-e135.

Wang, Q., Chen, R., Cheng, F., Wei, Q., Ji, Y., Yang, H., ... & Li, B. (2019). A Bayesian framework that integrates multi-omics data and gene networks predicts risk genes from schizophrenia GWAS data. *Nature neuroscience*, *22*(5), 691-699.

Wilson, M. D., Sethi, S., Lein, P. J., & Keil, K. P. (2017). Valid statistical approaches for analyzing sholl data: Mixed effects versus simple linear models. *Journal of neuroscience methods*, *279*, 33-43.

Xie, Z., Bailey, A., Kuleshov, M. V., Clarke, D. J., Evangelista, J. E., Jenkins, S. L., ... & Ma'ayan, A. (2021). Gene set knowledge discovery with enrichr. *Current protocols*, *1*(3), e90.

Zhao, G., Oztan, A., Ye, Y., & Schwarz, T. L. (2019). Kinetochore proteins have a post-mitotic function in neurodevelopment. *Developmental cell*, *48*(6), 873-882.

Figure Legends

Figure 1

Generation of Nrg1V_{321}L knock-in mice

(**A**) A schematic diagram of the *Nrg1* genomic structure. The *Nrg1* gene encodes six families of isoforms as a result of alternative promoter usage. Types I, II, IV and V contain an Ig-like domains (encoded by exons 3 & 4). Exon 7 is the unique 5-prime coding exon for Type III Nrg1, encoding an N-terminal, cysteine-rich transmembrane domain. Exon 8, in combination with exon 9 or 10, and various combinations of exons 11, 12, and 13, encodes an EGF-like domain common to all Nrg1 isoforms. Exon 13 encodes a common C-terminal transmembrane domain. The C-terminal intracellular domain is encoded by exons 14-17. The missense SNP that results in a valine-to-leucine substitution in the C-terminal transmembrane domain Is shown above the gene. (**B**) Schematic diagram of the BAC clone used for generating the target construct corresponding to a region of the Nrg1 gene that comprises the entire Type III coding region. Below the BAC clone is a diagram of the targeting construct, including a 5.8-kbp left homology arm, a neoR cassette in the antisense orientation flanked by Frt sites, and a 2.5-kbp right homology arm. (**C**) Diagram showing wildtype and mutant alleles (the mutant following flippase removal of the neo cassette). The C-terminal transmembrane domain sequence is underlined. Black arrows labeled "NDEL1" and "NDEL2" indicate approximate genomic locations of genotyping primers. (**D**) An example genotyping gel of offspring from a het x het cross illustrating a wildtype, heterozygote and homozygote. (**E**) The mutant mouse line was maintained by breeding heterozygotes. The genotype of pups from >100 litters was analyzed for deviation from the expected 1:2:1 ratio. No deviation was found.

Figure 2

V_{321}L mutation reduces nuclear back signaling in the hippocampus

(**A**) Immunoblot showing triplicate nuclear fractions isolated from pooled cortical and hippocampal lysates. Nrg1 ICD was detected using Santa Cruz Biotechnology antibody sc-348. Histone H3 served as a nuclear loading control, and Na+/K+ ATPase as a marker for the membrane fraction (N=3 mice/genotype). (**B**) Dissociated hippocampal neurons from P4 pups were cultured for 14 days in vitro, fixed, and stained for Prox1, βIII Tubulin, and counterstained with DAPI. Proportion of Prox1+ neurons was quantified by adding across 10 fields of view with βIII Tubulin+ cells per plating (N=5 mice pooled, 4 platings). Mann-Whitney Rank Sum Test p=0.0286. Scale bar=10μm. (**C**) Left, Hippocampal neurons from VV and LL neonatal pups (P4) were cultured for 17 days in vitro and were stimulated with either vehicle (Veh), 10nM sErbB4 (sB4), or 10nM sErbB4 with a 24h pre-treatment with 20μM DAPT (D). Neurons were fixed and stained using an antibody directed against the Nrg1-ICD and counterstained with DAPI. Scale bar=10μm. Right, Quantification of nuclear clusters of Nrg1-ICD. Neurons from VV mice show increased nuclear ICD clusters in response to B4 stimulation, which is counteracted by pretreatment with DAPT (D). Neurons from LL mice do not respond to sB4 stimulation (N= 6-13 neurons, 3 platings/mouse, 3 mice/genotype. One-way ANOVA p-values corrected for multiple comparisons using Tukey's posthoc test; VV Veh vs. VV sB4 p<0.0001; VV sB4 vs. VV sB4+DAPT p<0.0001; VV sB4 vs. LL Veh p<0.0001; VV sB4 vs. LL B4 p<0.0001. All other comparisons are statistically not significant).

Figure 2- supplement: Validation of new Nrg1 ICD antibody.

(A) Neuro2A (N2A) cells were transfected with a plasmid encoding C-terminally YFP-tagged full length Type III Nrg1-β1a. Both transfected and non-transfected cells were stained using the antibody developed in this study- Nrg1 ICD_{DAT} (See methods). Non-transfected (GFP-) cells did not stain by the new anti-ICD antibody. Scale bar=10μm. **(B)** N2A cells were either transfected with a plasmid encoding GFP (pMAX GFP) or YFP-tagged full length Type III Nrg1-β1a. Whole cell lysates were prepared 48h after transfection and probed on an immunoblot using the anti-Nrg1 ICD antibody used in panel A. Arrows indicate appropriate bands only detected in transfected cells corresponding to the full-length protein (FL) and ICD/TM-ICD (ICD). * denote non-specific bands. Ladder values are in kDa.

Figure 3

Transcriptomic analysis of V_{321}L DG

(**A**) Schematic and representative image of DG dissection from hippocampal slices; Mo= molecular layer, GCL= granule cell layer, Hi= hilus. (**B**) Volcano plot for differentially expressed genes between WT and MUT DG. Each datapoint represents a single gene. Colored points delineate fold change of at least 1.25 (blue dots – downregulated, red dots- upregulated) with an adjusted p-value <0.1, and dark colored points represent those with ANCOVA adjusted p-value <0.05. (N=6 mice/genotype. 3 Male/3 Female) (**C**) Statistically enriched functional terms from Ingenuity Pathway Analysis (IPA) for differentially expressed genes between VV and LL DGs. Arrows indicate enriched terms highlighting the presence of dendritic growth and branching and proliferation of neuronal cells- features chosen for further investigation in this manuscript. (**D**) Statistically significantly enriched disease terms from IPA for the differentially expressed gene list. Green bracket highlights cancer terms indicating the potential presence of genes involved in cell cycle regulation and magenta arrows highlight terms associated with psychotic and neurodevelopmental disorders. (**E**) Left, Immunohistochemical validation of downregulated DG marker genes Prox1 and Calb1 in WT and MUT. Right, Quantification of Prox1 and Calb1 immunoreactivity (signal density) in the granule cell layer of WT and MUT mice shows significant reduction in Prox1 (p=0.029, Mann-Whitney U=0) and Calb1 (p=0.029, Mann-Whitney U=0) protein expression in the MUT DG (N=4 mice/genotype) Scale bar=10μm.

Figure 3- Supplement: Enrichment analysis of potential transcriptional regulators of DEGs in V_{321}L mutant DG.

(**A**) Predicted transcriptional regulators from ENCODE and ChEA databases enriched for regulating upregulated genes in the MUT DG. **(B)** Predicted transcriptional regulators from ENCODE and ChEA databases enriched for regulating downregulated genes in the MUT DG.

Figure 4

Type III Nrg1 is expressed in the hippocampal neurogenic niche

(A) Fluorescent in situ hybridization of dentate gyrus from an adult mouse brain stained using probe directed towards Type III Nrg1 and counterstained with DAPI. Inset shows TypeIII Nrg1 is expressed in the subgranular zone (SGZ) as well as broadly across the granule cell layer (GCL). Scale bar= 100μm. MOL=molecular layer (**B**) **Left,** immunohistochemistry with NeuroMab antibody clone N126B/31, which targets the N-terminus of Type III Nrg1 (green), in a coronal section of the adult mouse hippocampal formation, counterstained with DAPI (blue). **Right,** high magnification of white dotted box showing Type III Nrg1-expressing cells (red arrows) residing in the subgranular zone (SGZ) of the dentate gyrus (DG). (**C**) Proliferating cells in the dentate gyrus were labeled with a systemic injection of EdU

(50µg EdU/g mouse) 24 hours prior to tissue harvest. Immunohistochemistry of Type III Nrg1 (green) revealed subpopulations of proliferating progenitors that express Type III Nrg1. Scale bar= 10µm. **(D)** Co-immunohistochemistry of Type III Nrg1 (green) and doublecortin (Dcx; red) in the dentate gyrus revealed subpopulations of neuroblasts that express Type III Nrg1. Scale bar= 10µm.

Figure 5

Proliferation is decreased in the $V_{321}L$ homozygous DG, but neuronal production is comparable to WT DG.

(A) Left, immunohistochemistry of Ki67 (green), a marker for proliferation, in the DG of P22 WT and MUT littermates and cagemates, merged with DAPI (blue) counterstain. Inset shows a higher magnification image with arrowheads indicating Ki67+ proliferating cells in the subgranular zone of the DG. **Right,** stereological quantification of Ki67+ populations in the DG of P21 WT and MUT (WT N= 5 mice, MUT N= 4 mice; p=0.0271, Welch's t-test. t=2.697, df=8.050). **(B) Left,** doublecortin (Dcx) immunoreactivity (green) merged with DAPI (blue) counterstain in DG of WT and MUT mice. Inset shows higher magnification image of the region delineated in the white box; arrowheads point to Dcx+ cells in the DG. **Right,** quantification of Dcx+ population from confocal images of subsampled, coronal DG sections. Confocal images were acquired in 3-µm z-steps from 20-µm coronal sections, and 4-10 images were quantified for each animal (P60-P180 WT N= 11 mice, MUT=10 mice, p= 0.9865, Welch's t-test. t=0.017, df=18.68). (**C) Left,** Neural progenitors in S phase of the cell cycle were labeled with EdU by intraperitoneal injection (50µg EdU/g body weight) in ~P90 animals. 24 hours post-injection, samples were harvested and processed to detect Ki67 immunoreactivity in cells that have reentered cell cycle. EdU and Ki67 co-immunoreactivity indicates cells that remained in the cell cycle 24 hours post-injection (yellow arrowheads). EdU immunoreactivity without Ki67 expression indicates cells that have exited the cell cycle (red arrowheads). Ki67 immunoreactivity alone indicates cells that were not in S phase at the time of injection but were in the cell cycle at the time of tissue harvest. **Right,** Quantification of cell cycle reentry by computing the proportion of cells that remained in the cell cycle (EdU+ Ki67+) out of all cells in S phase of the cell cycle at the time of labeling (EdU+ cells). Epifluorescent images were acquired in 1-µm z-steps from 20-µm coronal sections, and 12-14 sections were quantified for each animal (WT N= 6 mice, MUT N=5 mice, p= 0.0043, Mann-Whitney Rank Sum Test U=0). (**D) Left,** DG neural stem cells were infected with a replication-deficient GFP-expressing retrovirus via stereotaxic injection, followed by 14 days of incubation to label NPs and their progeny. The identity of GFP+ cells were determined by a combination of morphology, Dcx immunoreactivity, and Nissl staining. Neural progenitors (NPs) were identified by the lack of radially oriented processes with or without Dcx immunoreactivity (open arrowheads). Immature granule cells (iGCs) were identified by their radially oriented neurites, Dcx+ and Nissl+ staining (filled, yellow arrowheads). Astrocytes were identified by their star-like morphology and lack of Dcx immunoreactivity and Nissl staining (yellow arrows). **Right,** Fate specification was quantified as proportion of GFP+ cells that remained radial glial-like stem cells, NPs, or committed to neuronal or astroglial fates. 5-14 50-µm sections were quantified from each animal, depending on infection efficiency (WT N=3 mice, MUT N=4 mice; Two-way ANOVA Genotype x Cell Fate p=0.0003 F(3, 20)=9.864. NP, WT vs. MUT Bonferroni-corrected p=0.0026. iGC, WT vs. MUT Bonferroni-corrected p=0.0069. RGL & Astrocyte comparisons between genotypes were not significant p>0.9999).

Figure 5- Supplement: Enhanced survival of progenitors in the $V_{321}L$ mutant DG.

Left, Animals (PND90) were intraperitoneally injected with 3 pulses of EdU (50µg EdU/g mouse) 24 hours apart. Tissue was then harvested 1 month after the first injection to assess survival of proliferative populations in the DG. EdU was visualized by click chemistry. The DG ultrastructure is visualized by DAPI (blue) counterstain. **Right,** Quantification of EdU+ cells from DG coronal sections. Epifluorescent images were acquired in 1-µm z-steps from 20-µm coronal sections, and 13-14 sections were quantified for each animal (wildtype N= 4 mice, mutant N=4 mice, p= 0.6792, Welch's t-test).

Figure 6

Neurons produced in the $V_{321}L$ homozygous DG display aberrant dendritic arborization.

(A) Left, Doublecortin (Dcx - green) immunohistochemistry in the P72 DG along with DAPI counterstain (blue), with high magnification of the dotted white boxes to the right displayed in greyscale for better visibility. **Right,** Representative tracings of Dcx+ cells in WT and MUT DG. **(B)** Representative tracings of Golgi-impregnated DG granule cells from ~P60 WT and MUT. Neurites are color coded by branch order (1°= red, 2°= orange, 3°= yellow, 4°= green, 5°= blue, 6°= purple, 7°= pink). **(C) Top,** schematic of Sholl analysis on a representative neuronal tracing. **Bottom,** Length of dendritic segments within each zone were summed. Sholl analysis reveals difference in distribution of dendritic lengths in MUT mice. Shaded region around the line represents standard deviation. Data is compiled from 11 neurons from 5 WT animals and 13 neurons from 5 MUT at ~P60. (Mixed effects model Two-way RM ANOVA Genotype x Distance from soma #p=0.0347, F(16, 352)=1.763 ; WT vs. MUT at 80µm away from soma FDR corrected *q=0.0511). **(D)** Quantification of dendritic lengths by branch order reveals altered complexity in arbors of $V_{321}L$ homozygous mutants. Two-way ANOVA Genotype x Branch order p=0.0118, F(6, 154)=2.845. 5th order branch, WT vs. MUT Bonferroni corrected p=0.055. All other comparisons between genotypes were not significant (4th order p=0.098; all other orders p>0.9999). **E.** Proportion of neurons in which 5th, 6th, and 7th order branching are present. MUT granule cells had fewer branches at the higher orders of branching (5th order, p=0.0131; 6th order, p= 0.0817; 7th order, p=0.458; Fisher's exact test).

Figure 6- Supplement 1: Total dendritic length trends higher in LL mutant DG granule cells.

(A) Total dendritic length of Golgi-impregnated granule cells quantified using NeuronStudio. Total dendritic length trends greater in LL mutants, though not statistically significant (p= 0.252, Wilcoxon rank sum test). **(B)** Total number of branch points trends lower in LL DGs compared to wildtype counterparts, although the difference is not statistically significant (p= 0.446, Welch's t-test).

Figure 6- supplement 2: **$V_{321}L$ mutant cortical neurons show selective loss of ErbB4 induced dendrite growth.**

(A) Cortical neurons from embryonic VV and LL mice (E18.5) were cultured for 3 days invitro and were stimulated with soluble ErbB4 (B4), PI3K inhibitor Wortmannin (WM), L6 (gamma secretase inhibitor), WM+B4, or L6+B4. Neurons were fixed and axonal length was quantified. (**Navy blue boxes =WT**; axonal length: One-way ANOVA WT NT v. WT sB4 p=0.0002, WT L6 v. WT L6+B4 p<0.0001; **light blue boxes=MUT**; axonal length: One-way ANOVA MUT NT v. MUT sB4 p=0.0014, MUT L6 v. MUT L6+sB4 p=0.0289) **(B)** Treatment and conditions same as in A., quantification is for dendritic length. (**Navy blue boxes =WT;** dendrite length: One-way ANOVA dendritic length: WT NT v. WT B4 p=0.0019, WT WM v. WT WM+B4 p<0.0001; **light blue boxes=MUT;** dendrite length: MUT NT v. MUT B4 p>0.9999).

Figure 7

Dysregulation of a schizophrenia-susceptibility gene network in the $V_{321}L$ DG.

- **(A) Left,** Orthologs of genes associated with schizophrenia spectrum disorders (in IPA) were found to be dysregulated in the MUT DG. **Right,** Visualization of the network grown by seeding schizophrenia-related dysregulated genes (left) along with the remaining set of differentially expressed genes between

WT and MUT DG in IPA. Node colors represent fold change in expression according to heatmap. **(B)** Gene ontology analysis of the gene network in A showing enrichment of several known schizophrenia-related features indicating that genes relevant to disease-associated features are dysregulated in the mutant DG. **(C)** Top 10 hub genes identified by mean clique clustering (MCC) analysis of the network shown in A are all part of the originally identified schizophrenia-related gene set. Colors represent Hub rank, Rank 1=red, Rank 10= yellow. **(D)** Network display of 10 hub genes identified in B, along with their first-degree neighbors (lavender nodes) shows a hub-spoke connectivity with schizophrenia related genes forming hubs.

Figure 1

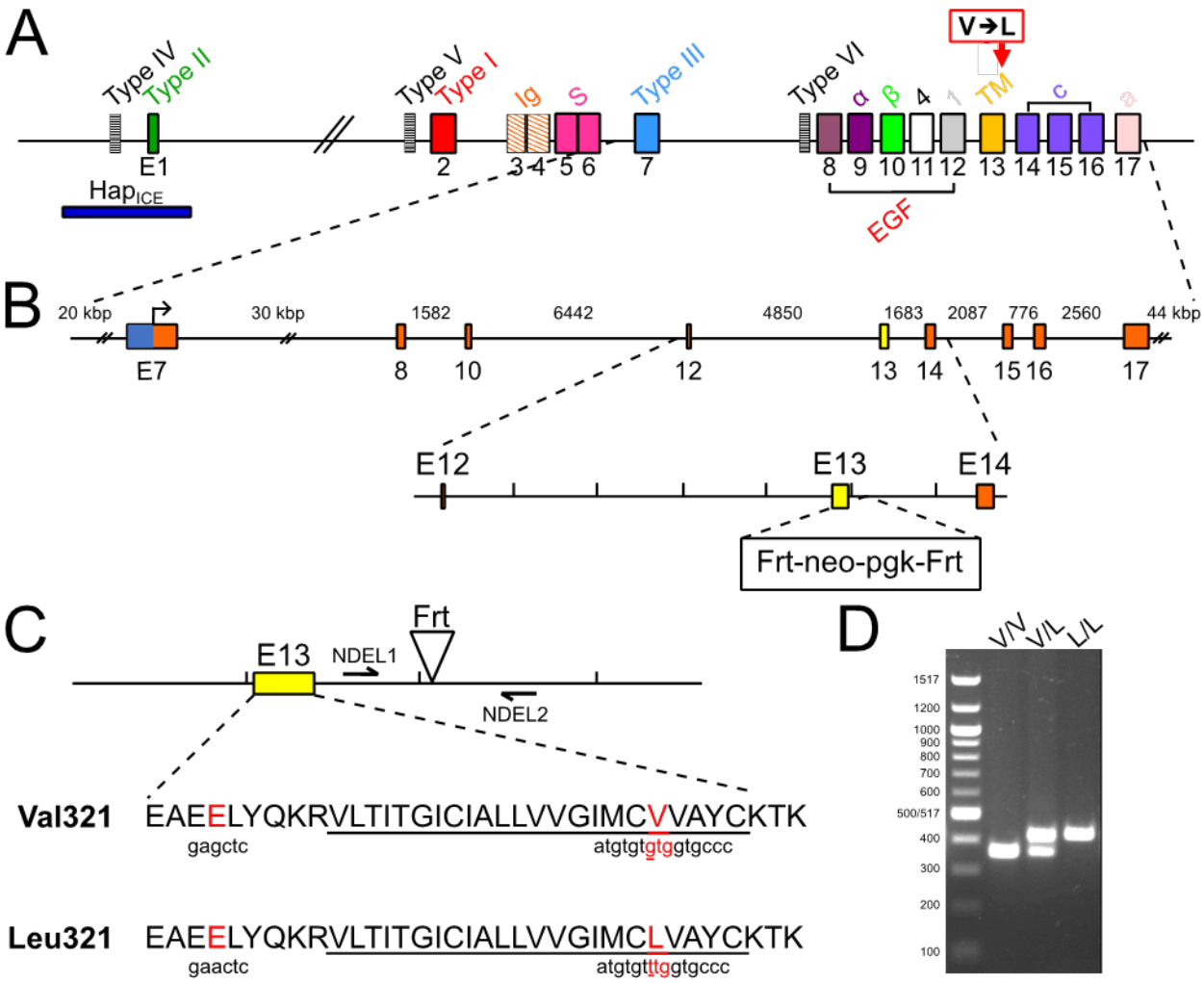

E

Genotype	Observed	Expected	
V/V	202	213.5	
V/L	439	427	
L/L	213	213.5	
		X^2 = 0.958	p= 0.6195

Figure 2

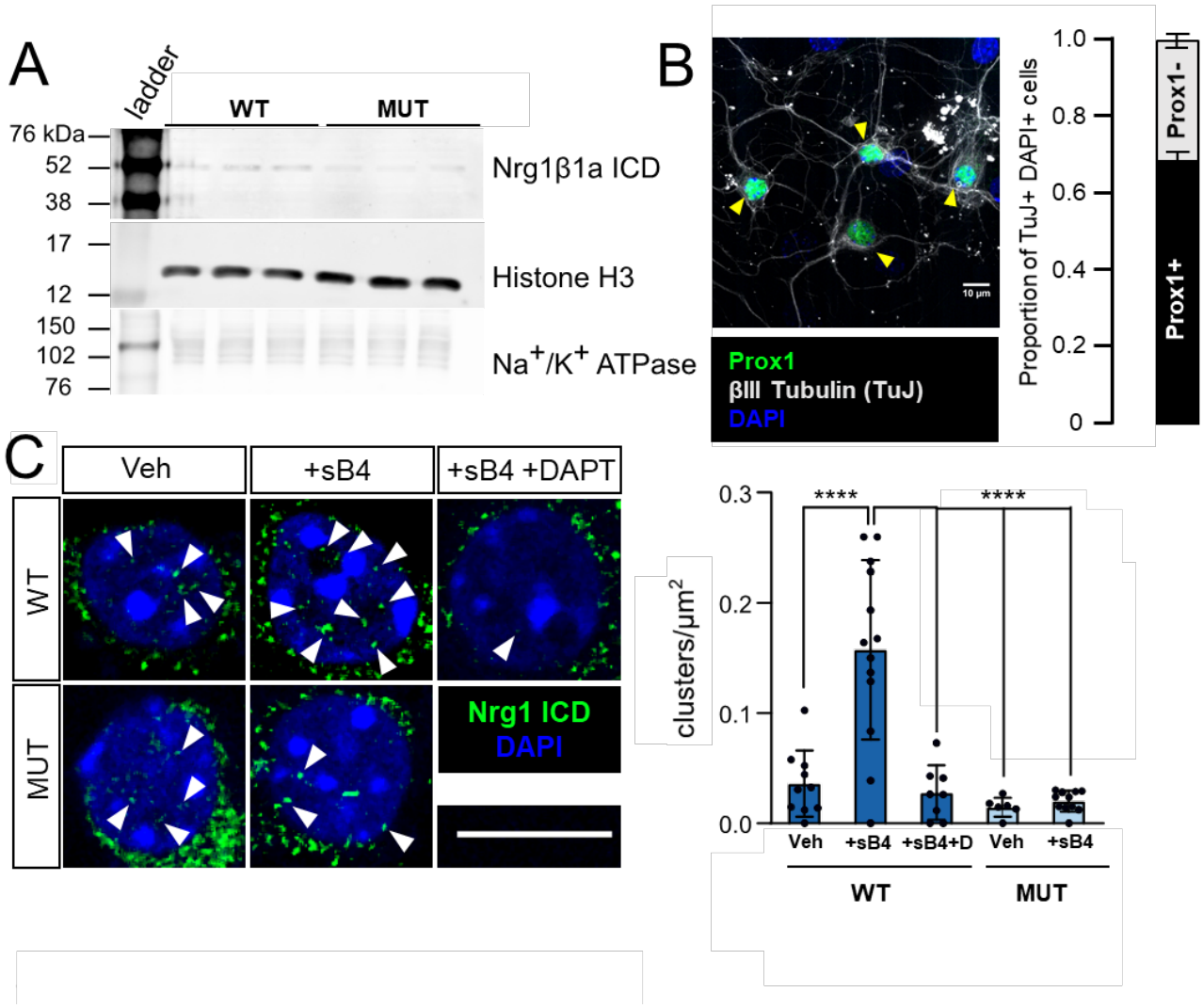
A
ladder
WT
MUT
76 kDa
52
38
17
12
150
102
76
Nrg1β1a ICD
Histone H3
Na+/K+ ATPase
B
Prox1
βIII Tubulin (TuJ)
DAPI
10 µm
Proportion of TuJ+ DAPI+ cells
1.0
0.8
0.6
0.4
0.2
0
Prox1-
Prox1+
C
Veh
+sB4
+sB4 +DAPT
WT
MUT
Nrg1 ICD
DAPI
clusters/µm2
0.3
0.2
0.1
0.0
****
****
Veh
+sB4
+sB4+D
Veh
+sB4
WT
MUT

Figure 2 – Supplement 1

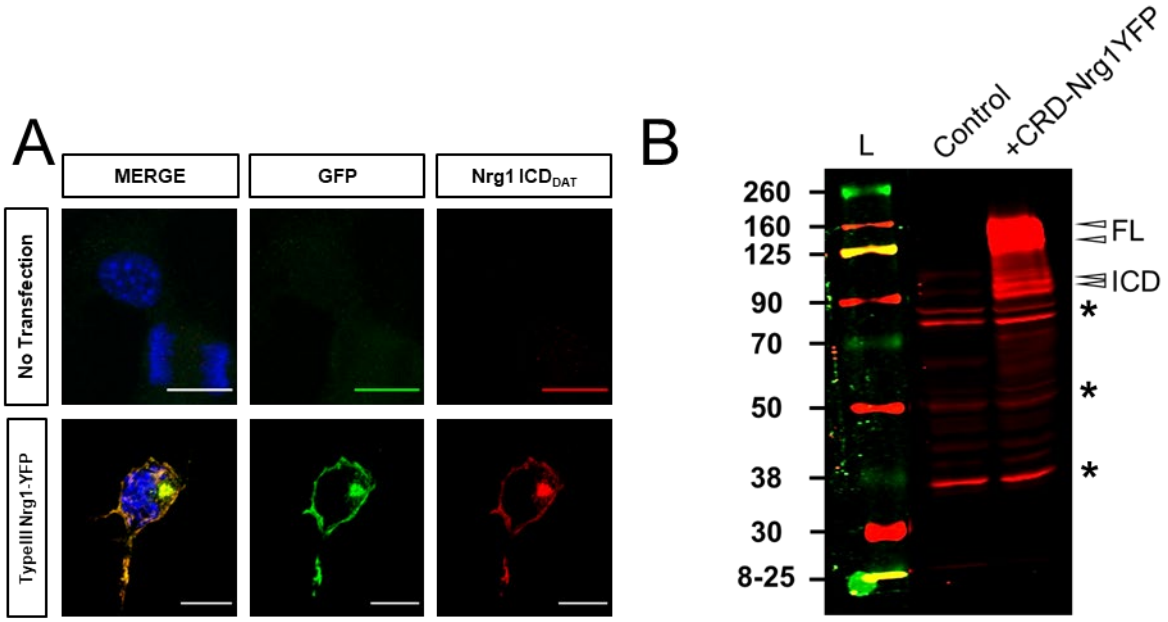

Figure 3

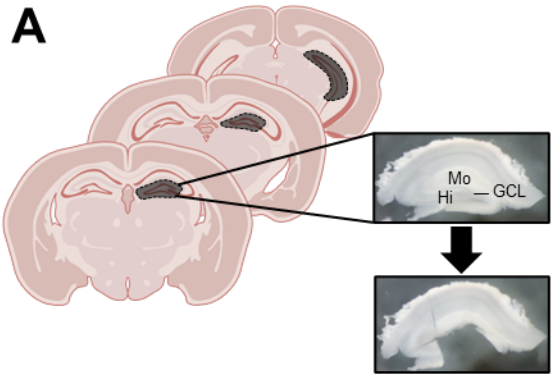

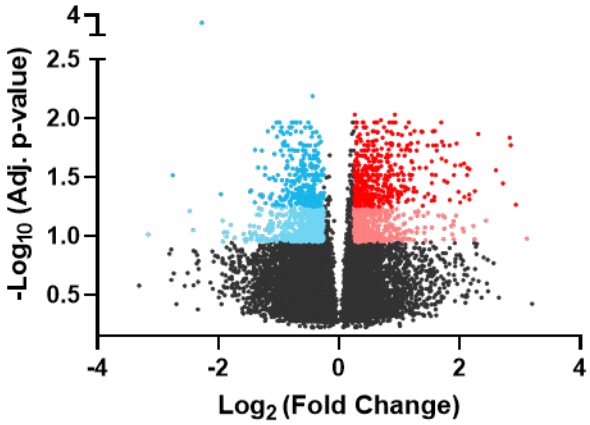

C

NEURONAL DEVELOPMENT - RELATED

GO- Functions	p-value
Development of neurons	1.27E-14
⇨ Neuritogenesis	9.59E-10
Neurotransmission	1.64E-09
⇨ Branching of neurites	1.36E-07
Morphology of hippocampus	1.66E-07
⇨ Formation of dendrites	2.39E-07
⇨ Dendritic growth/branching	4.25E-07
Growth of neurites	1.28E-06
⇨ Proliferation of neuronal cells	3.56E-06
Developmental process of synapse	3.65E-06
Density of neurons	6.33E-06
Quantity of neurons	8.52E-06
⇨ Formation of dendritic spines	2.01E-05
Morphology of granule cell layer	2.93E-05
Guidance of axons	4.56E-05
Density of synapse	1.10E-04
Maturation of neurons	1.67E-04
⇨ Differentiation of neurons	2.30E-04
⇨ Growth of axons	2.31E-04

D

CANCER RELATED

[PSYCHOSIS/NEURODEV.] DISORDER RELATED

GO- Disease-related	p-value
Cancer	1.71E-53
Brain tumor	1.28E-26
Brain glioma	1.29E-26
Cancer of cells	9.30E-17
Movement Disorders	4.29E-11
Neurological signs	2.92E-10
Disorder of basal ganglia	1.56E-07
⇨ Pervasive developmental disorder	6.05E-07
Abnormal morphology of hippocampus	8.53E-07
⇨ Schizophrenia	1.35E-06
Seizures	1.10E-05
Cognitive impairment	1.19E-05
⇨ Schizoaffective disorder	2.08E-05
⇨ Bipolar disorder	3.53E-05
⇨ Familial neurodevelopmental disorder	5.58E-05
Abnormal morphology of cerebellum	6.00E-05
Abnormal morphology of granule cell layer	9.09E-05
Brain developmental abnormality	1.74E-04
Multiple Sclerosis	2.19E-04
Early-onset neurological disorder	2.56E-04
⇨ Neurodevelopmental disorder	2.83E-04
⇨ Sporadic schizophrenia	4.83E-04

E

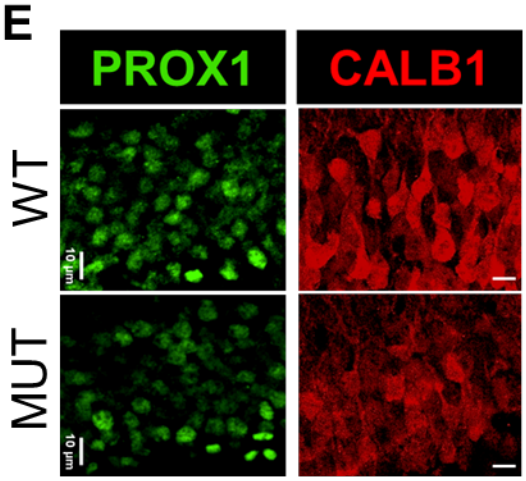

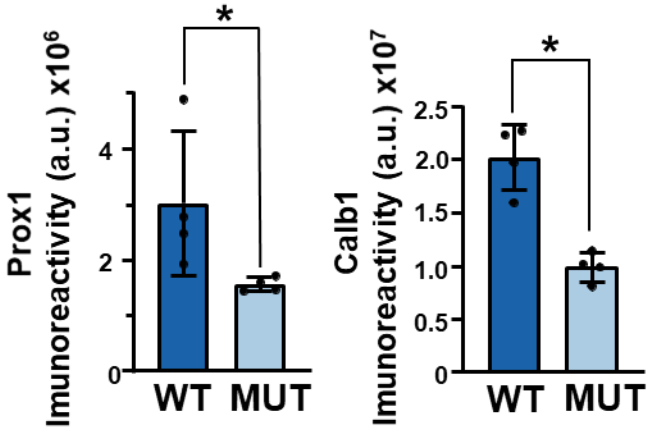

Figure 3- Supplement 1

A

Upregulated Genes

Term	Adjusted P-value
SUZ12 CHEA	3.26E-15
REST CHEA	7.65E-07
CTCF ENCODE	4.86E-06
REST ENCODE	1.28E-04
SMAD4 CHEA	2.72E-04
EZH2 CHEA	2.26E-03
SMC3 ENCODE	3.45E-03
RAD21 ENCODE	2.74E-02
NFE2L2 CHEA	4.52E-02

B

Downregulated Genes

Term	Adjusted P-value
E2F4 ENCODE	3.73E-10
TAF1 ENCODE	5.63E-04
UBTF ENCODE	8.07E-04
ZNF384 ENCODE	6.07E-03
MAX ENCODE	6.07E-03
SIN3A ENCODE	1.04E-02
EGR1 ENCODE	4.03E-02

Figure 4

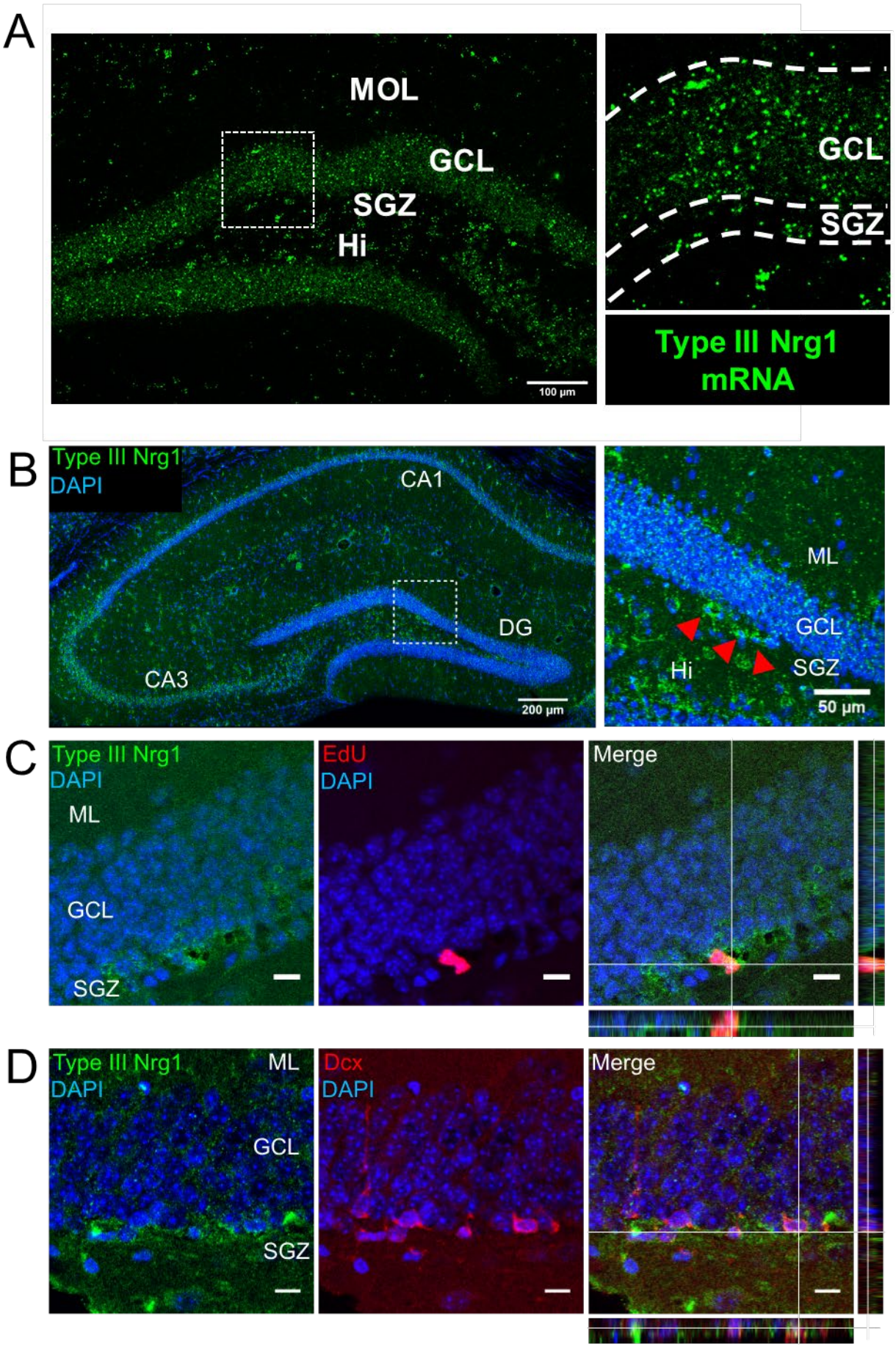
A
MOL
GCL
SGZ
Hi
100 µm
GCL
SGZ
Type III Nrg1
mRNA
B
Type III Nrg1
DAPI
CA1
DG
CA3
200 µm
ML
GCL
Hi
SGZ
50 µm
C
Type III Nrg1
DAPI
ML
GCL
SGZ
EdU
DAPI
Merge
D
Type III Nrg1
DAPI
ML
GCL
SGZ
Dcx
DAPI
Merge

Figure 5

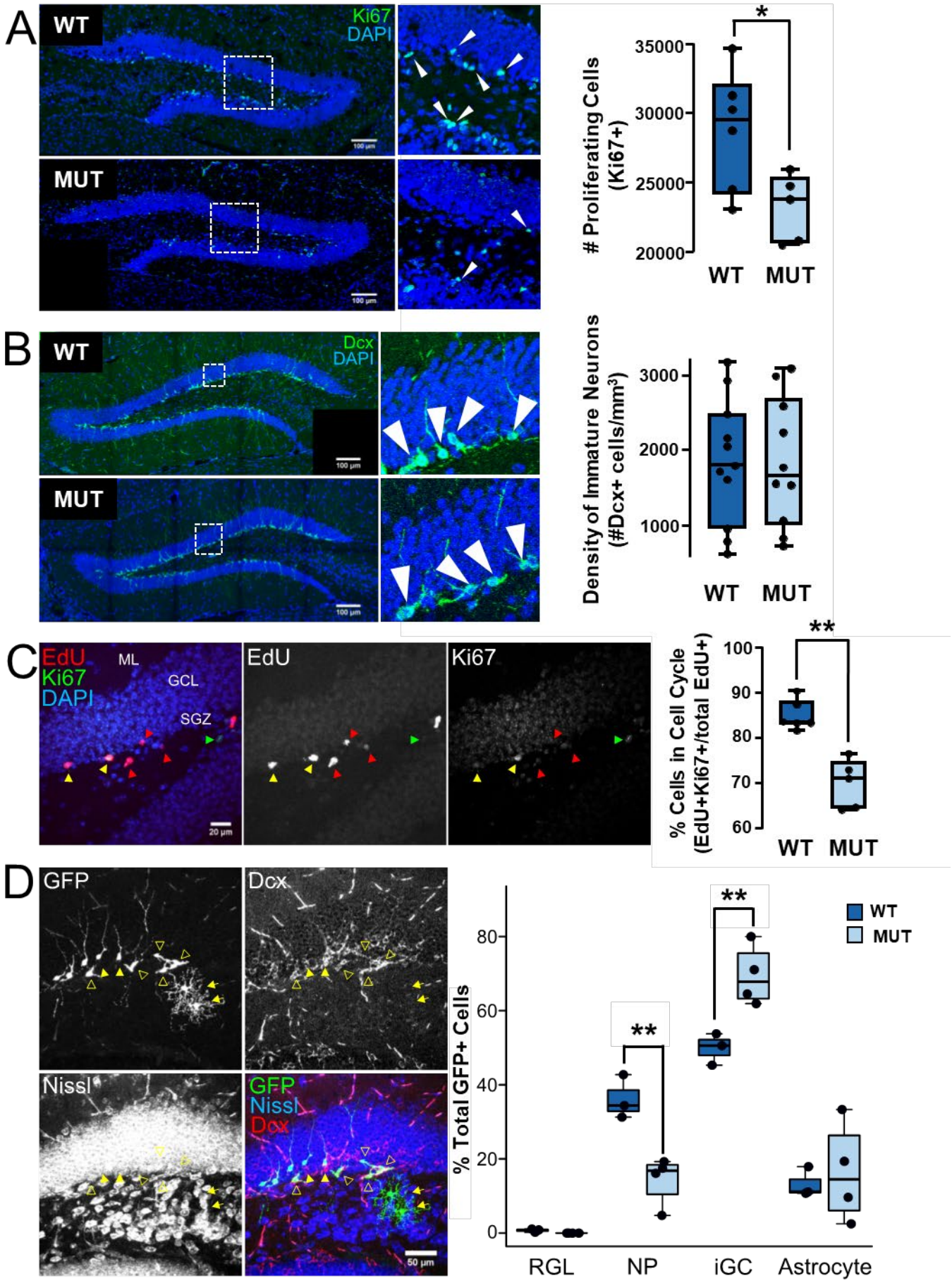
A
WT
Ki67
DAPI
MUT
Proliferating Cells (Ki67+)
35000
30000
25000
20000
*
WT
MUT
B
WT
Dcx
DAPI
MUT
Density of Immature Neurons (#Dcx+ cells/mm³)
3000
2000
1000
WT
MUT
C
EdU
Ki67
DAPI
ML
GCL
SGZ
EdU
Ki67
% Cells in Cell Cycle (EdU+Ki67+/total EdU+)
100
90
80
70
60
**
WT
MUT
D
GFP
Dcx
Nissl
GFP
Nissl
Dcx
% Total GFP+ Cells
80
60
40
20
0
**
**
WT
MUT
RGL
NP
iGC
Astrocyte

-

Figure 5 – Supplement 1

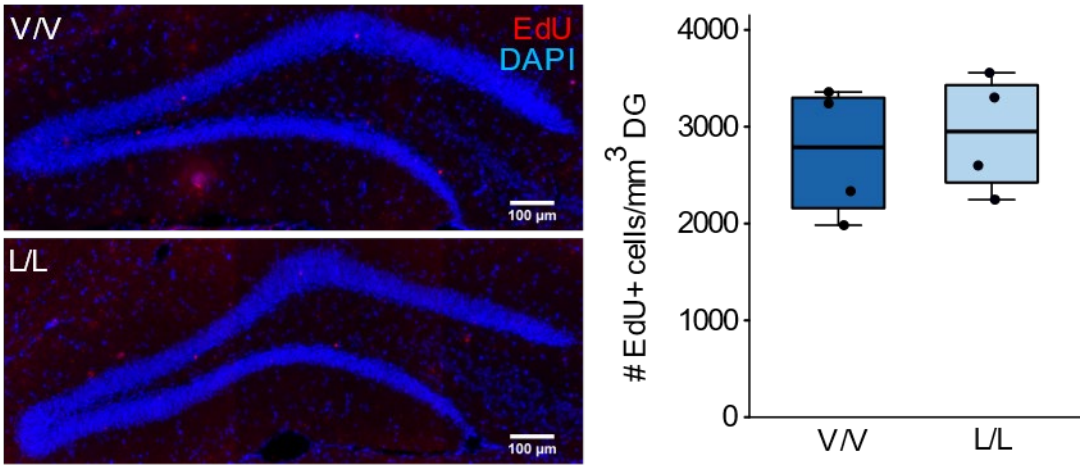

Figure 6

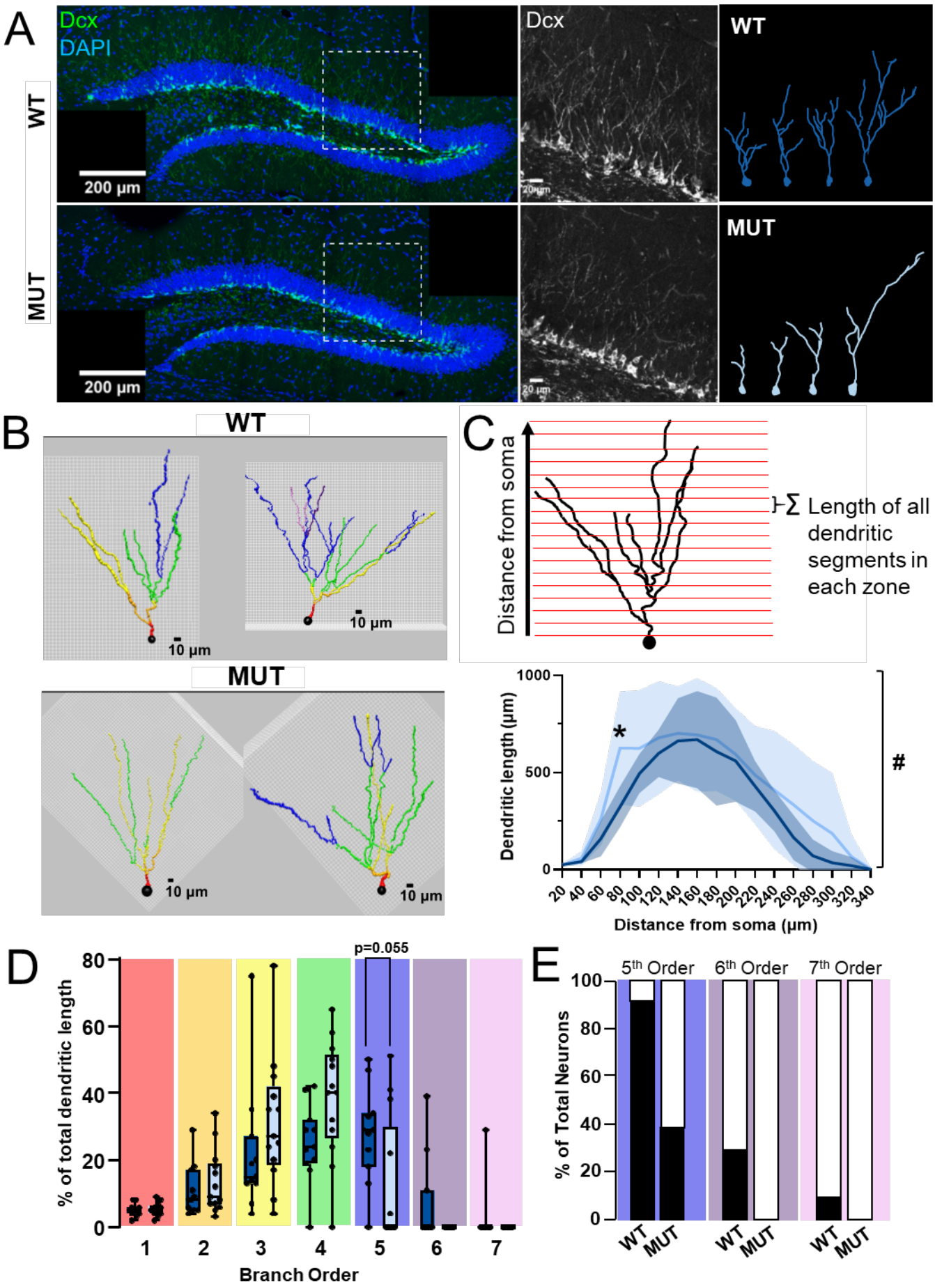
A
Dcx
DAPI
WT
MUT
200 µm
200 µm
Dcx
20µm
20 µm
WT
MUT
B
WT
MUT
10 µm
10 µm
10 µm
10 µm
C
Distance from soma
Σ Length of all dendritic segments in each zone
Dendritic length (µm)
1000
500
0
*
#
20 40 60 80 100 120 140 160 180 200 220 240 260 280 300 320 340
Distance from soma (µm)
D
% of total dendritic length
80
60
40
20
0
p=0.055
1 2 3 4 5 6 7
Branch Order
E
5th Order
6th Order
7th Order
% of Total Neurons
100
80
60
40
20
0
WT MUT
WT MUT
WT MUT

Figure 6 – Supplement 1

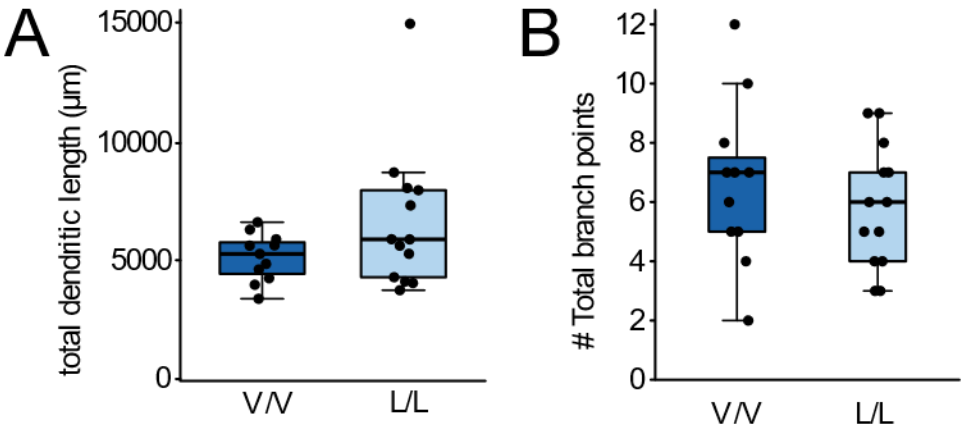

Figure 6 – Supplement 2

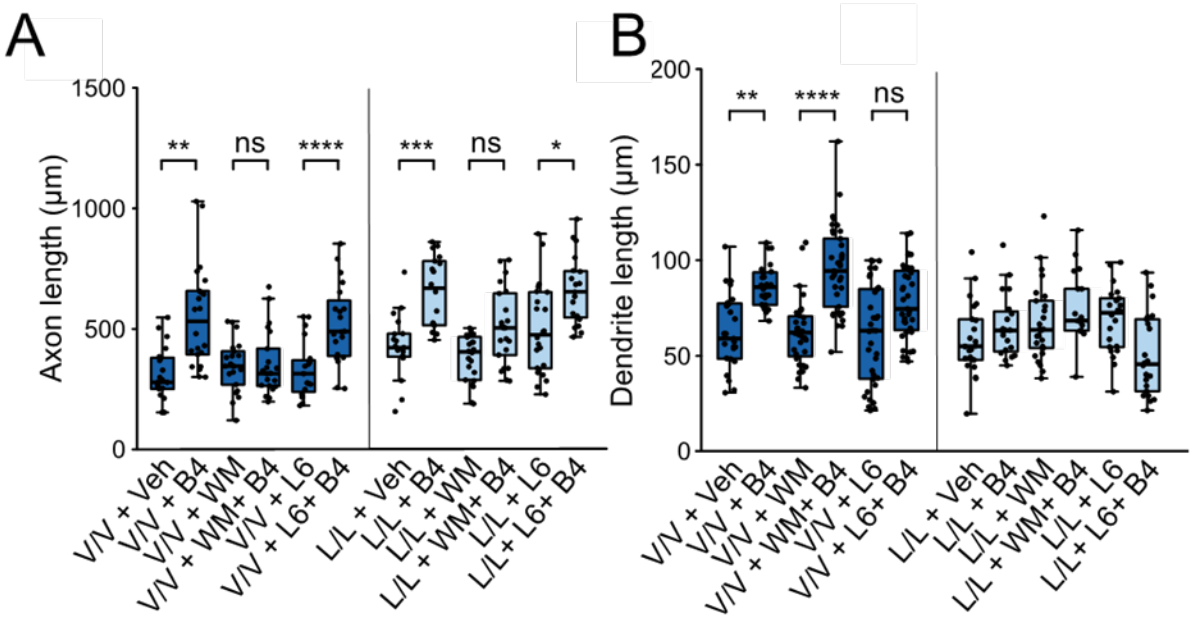

Figure 7

A

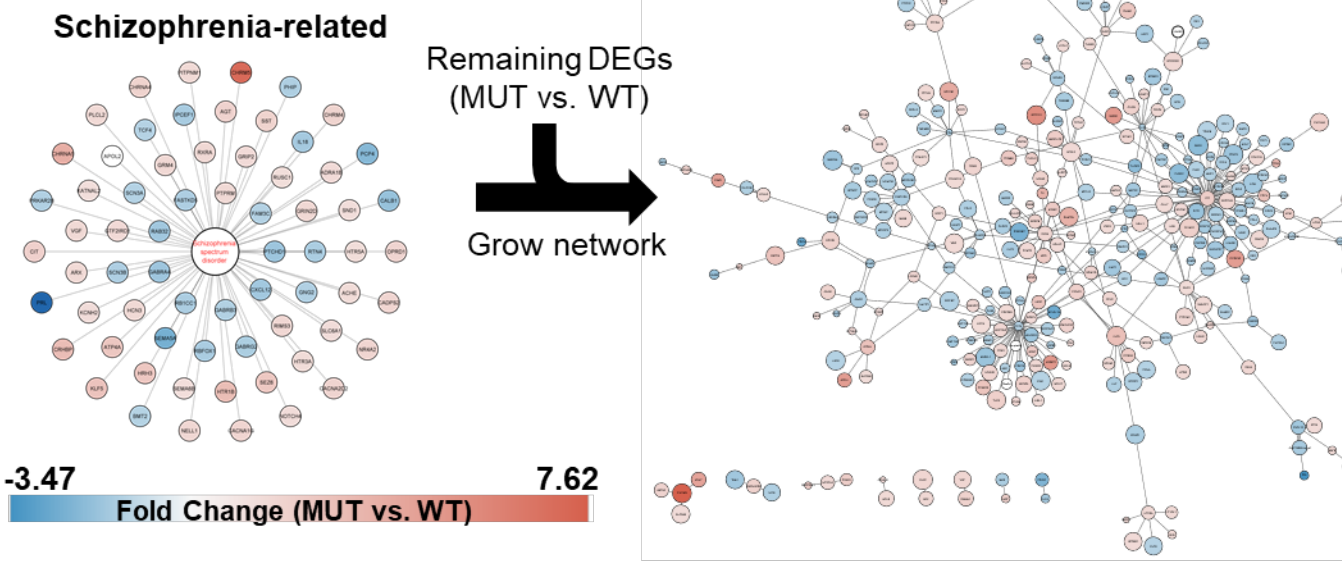

B

GO- Pathway Enrichment

Term	p-value
Human cytomegalovirus infection	9.23E-04
➡ Cholinergic synapse	1.25E-03
Cell cycle	1.93E-03
GABAergic synapse	4.45E-03
Kaposi sarcoma-associated herpesvirus infection	9.44E-03
Apelin signaling pathway	9.44E-03
Pathways in cancer	9.44E-03
➡ Nicotine addiction	9.44E-03
➡ Glutamatergic synapse	9.44E-03
Retrograde endocannabinoid signaling	1.06E-02
➡ Chemokine signaling pathway	1.41E-02
Transcriptional misregulation in cancer	1.41E-02
Serotonergic synapse	2.80E-02
➡ PI3K-Akt signaling pathway	4.55E-02
Prolactin signaling pathway	4.55E-02
➡ Dopaminergic synapse	4.55E-02
AGE-RAGE signaling pathway in diabetic complications	4.55E-02
cGMP-PKG signaling pathway	4.55E-02

C

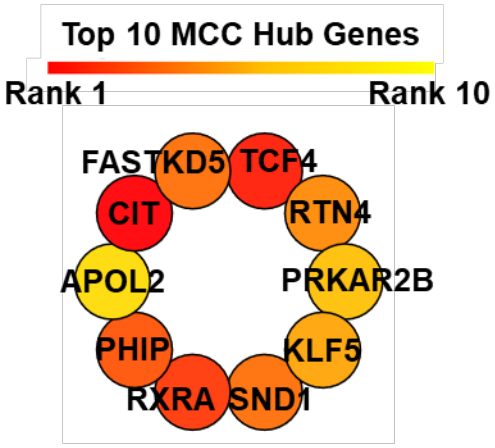
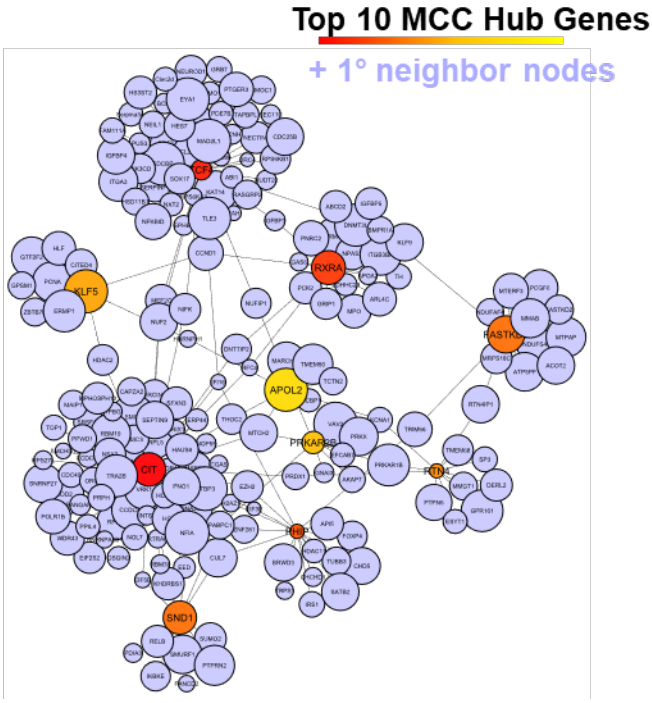
D